Lithos 151 (2012) 17–34

Contents lists available at ScienceDirect

Lithos

journal homepage: www.elsevier.com/locate/lithos

Petrogenesis of the igneous Mucajaí AMG complex, northern Amazonian craton — Geochemical, U–Pb geochronological, and Nd–Hf–O isotopic constraints

A.P. Heinonen [a,*], L.M. Fraga [b], O.T. Rämö [a], R. Dall'Agnol [c], I. Mänttäri [d], T. Andersen [e]

[a] Department of Geosciences and Geography, University of Helsinki, Finland
[b] CPRM, Geological Survey of Brazil, Rio de Janeiro, RJ, Brazil
[c] Instituto de Geociências, Federal University of Pará, Belém, PA, Brazil
[d] Research Laboratory, Geological Survey of Finland, Espoo, Finland
[e] Department of Geosciences, University of Oslo, Norway

ARTICLE INFO

Article history:
Received 30 January 2011
Accepted 22 July 2011
Available online 30 July 2011

Keywords:
Brazil
Rapakivi granites
Anorthosites
Isotope geology
Geochemistry
Petrogenesis

ABSTRACT

The ca. 1525 Ma igneous Mucajaí anorthosite–monzonite–granite (AMG) complex in northern Brazil is a rare manifestation of Mesoproterozoic intraplate magmatism in the northern Amazonian Craton. The complex comprises a two-phase rapakivi granite batholith with subordinate quartz–fayalite monzonites and syenites and the closely associated Repartimento anorthosite. Zircon U–Pb (ID–TIMS) geochronology reveals that the anorthosite (1526 ± 2 Ma), monzonite (1526 ± 2 Ma), and the main-phase biotite–hornblende granite (1527 ± 2 Ma) of the complex intruded the Paleoproterozoic (~1.94 Ga) country rocks simultaneously at ~1526 Ma and that the more evolved biotite granite is marginally younger at 1519 ± 2 Ma. Intraplate magmatism in the Mucajaí region was relatively short-lived and lasted 12 million years (1529–1517 Ma) at maximum. The Nd (whole-rock, ID–TIMS; ε_{Nd} from −1.9 to −2.8), Hf (zircon, LAM-ICP-MS; ε_{Hf} from −2.0 to −3.1), and O (zircon, SIMS; $\delta^{18}O$ from 6.1 to 7.0‰) isotopic compositions of the studied rocks are fairly uniform but still reveal a small degree of isotopic heterogeneity in the Paleoproterozoic crust enclosing the complex. The small isotopic differences observed in the two types of rapakivi granites (biotite–hornblende granite and biotite granite) may result either from an isotopically heterogeneous lower crustal source or, more likely, from contamination of the granitic magma derived from a lower crustal source during prolonged residence at upper crustal levels.

1. Introduction

Occurrences of Proterozoic intraplate magmatism characterized by the so-called anorthosite–mangerite–charnockite–granite (AMCG) suite are known from nearly all Proterozoic terranes on Earth (e.g., Ashwal, 1993). Typical localities include for example the Nain suite (in Labrador, eastern Canada; Emslie et al., 1994) and the *locus classicus* rapakivi granite association in southern Finland, Sweden, the Baltic countries, and far northwest Russia (Rämö and Haapala, 2005, and references therein). Massif-type anorthositic rocks (anorthosite ± olivine-bearing leucogabbroic rocks; Ashwal, 1993) represent the major basic magmatic member, whereas charnockitic rocks and ferroan (Frost and Frost, 2011) rapakivi granites typify the felsic phase of these suites (e.g., Bonin, 2007). Despite long-standing research efforts, the primary sources of the parental liquids for the rock groups are still not agreed upon (e.g., Bonin, 2007; Longhi, 2005; Morse, 2006). They have been suggested to be derived from the crust (e.g., Duchesne et al., 1999; Longhi, 2005), the mantle (e.g., Frost and Frost, 1997; Frost et al., 2002), or by different combinations of juvenile mantle and recycled crustal material (e.g., Emslie et al., 1994; Rämö and Haapala, 2005).

The ~4000 km^2 Mucajaí AMG complex (Fig. 1a; Fraga et al., 2009a) in Roraima (Brazil) is a part of a northwest trending ~900-km-long belt of rapakivi granite intrusions in the northern Amazonian Craton (Dall'Agnol et al., 1999). Besides Mucajaí, these rocks comprise the rapakivi granite of Parguaza (Fig. 1b; Gaudette et al., 1978; Mendoza, 1975) in Venezuela, and the Surucucus suite (Fig. 1b; Dall'Agnol et al., 1975; Pinheiro et al., 1981) on the border between Venezuela and Brazil. The igneous rocks in these suites are similar in age ranging from 1.55 to 1.53 Ga (Fraga et al., 2009a; Gaudette et al., 1978, 1996; Santos et al., 1999, 2003) and they have been interpreted to represent a single intraplate magmatic event (the Parguaza event, Gaudette et al., 1978) in the northern Amazonian craton (e.g., Dall'Agnol et al., 1999).

The amount of anorthositic rocks associated with the Mesoproterozoic north Brazilian rapakivi granites is notably smaller than in similar associations elsewhere (e.g., in Labrador; Ashwal, 1993). However, a prominent occurrence of massif-type anorthosite – the Repartimento anorthosite – is found associated with the rapakivi granites of the Mucajaí complex (Brandão and Freitas, 1994; Fraga et al., 2009a; Santos

* Corresponding author.
E-mail address: aku.heinonen@helsinki.fi (A.P. Heinonen).

0024-4937/$ – see front matter © 2011 Elsevier B.V. All rights reserved.
doi:10.1016/j.lithos.2011.07.016

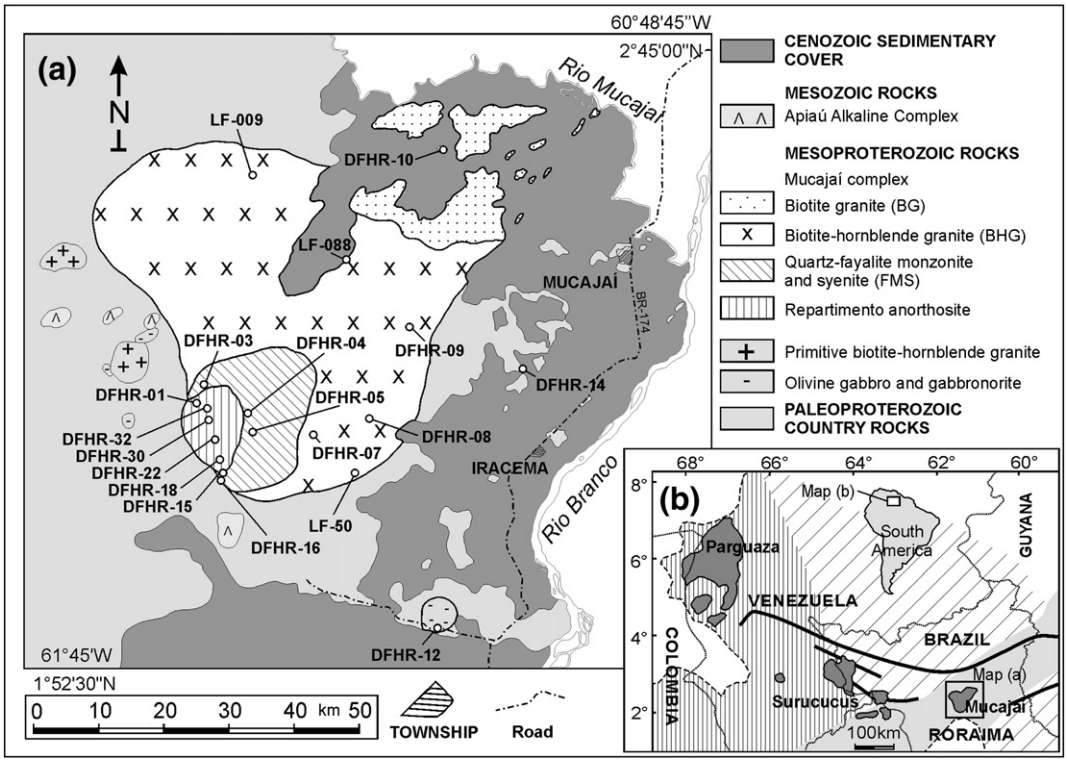

Fig. 1. (a) Geological map of the study area with sampling localities. (b) Regional map showing the location of the study area and the extent of the northern Amazonian rapakivi magmatism spanning from Roraima, Brazil (Mucajaí) through the border of Venezuela and Brazil (Surucucus) to the Colombian border in the west (Parguaza). Proterozoic geochronological provinces according to Santos et al. (2000, 2006) mentioned in the text are also shown: inclined hatching = Tapajós-Parima, vertical hatching = Rio Negro, gray fill = K'Mudku. Thick black lines trace the Cauarane–Coeroene belt of Fraga et al. (2009b). For further details and discussion on the geochronological provinces of the Guyana shield, see Fraga et al. (2009b). Inset shows a map of South America with the location of enlarged area in (b). Maps are adapted from Fraga et al. (2009a,b).

et al., 1999). The apparent intraplate features and the presence of massif-type anorthosite make the Mucajaí AMG complex a prime target for petrogenetic and comparative studies of Mesoproterozoic within-plate magmatism in northern Amazonia. Regardless of these apparent similarities with the classical AMCG suites (e.g., Fraga et al., 2009a) in this study we have adopted the descriptive AMG (Anorthosite–Monzonite–Granite) term for the Mucajaí complex.

We present whole-rock major, trace element, and Sm–Nd isotopic analyses, U–Pb ID–TIMS zircon geochronology, and O and Lu–Hf isotope compositions of zircons for the main rock types of the Mucajaí complex. These data constrain the petrogenetic and temporal relations of the different rock-types in the Mucajaí AMG complex and are used to characterize the intraplate rapakivi magmatism of the northern Amazonian craton and compare it to other similar localities around the world.

Table 1
Sampling and methods.

Sample	Rock type	Locality	Coordinates[a]		Geochemistry	U–Pb	Sm–Nd	Oxygen	Lu–Hf
			N	W	WR	Zircon	WR	Zircon	Zircon
					ICP-AES/MS	TIMS	TIMS	SIMS	LAM-ICP-MS
DFHR-01[b]	Anorthosite	Repartimento	2° 14.516	61° 31.564		x	x	x	x
DFHR-03	Monzonite	Mucajaí	2° 14.875	61° 31.423	x				
DFHR-04[b]	Monzonite	Mucajaí	2° 12.808	61° 25.654		x	x	x	x
DFHR-07	Biotite–hornblende granite	Mucajaí	2° 12.372	61° 20.886	x				
DFHR-08[b]	Biotite–hornblende granite	Mucajaí	2° 12.372	61° 20.886	x	x	x	x	x
DFHR-09	Biotite–hornblende granite	Mucajaí	2° 19.371	61° 13.633	x				
DFHR-10[b]	Biotite granite	Mucajaí	2° 35.382	61° 10.554		x	x	x	x
DFHR-12[b]	Gabbronorite	Caracaraí	1° 55.745	61° 10.882	x		x		
DFHR-14[b]	Gabbronorite	Country rock	2° 16.955	61° 02.903			x		
DFHR-15	Monzodiorite	Repartimento	2° 08.143	61° 28.947	x				
DFHR-16	Monzodiorite	Repartimento	2° 07.360	61° 29.415	x				
DFHR-18	Syenogranite	Repartimento	2° 08.718	61° 28.586	x				
DFHR-22	Anorthosite, coarse	Repartimento	2° 09.802	61° 29.046	x				
DFHR-30A	Anorthosite	Repartimento	2° 12.635	61° 30.725	x				
DFHR-30B	Anorthosite	Repartimento	2° 12.635	61° 30.725	x				
DFHR-32	Leuconorite, coarse	Repartimento	2° 13.670	61° 30.590	x				
LF-09A	Biotite–hornblende granite	Mucajaí	2° 33.526	61° 25.450	x				
LF-50	Monzonite	Mucajaí	2° 08.584	61° 19.297	x				
LF-88	Biotite-hornblende granite	Mucajaí	2° 26.813	61° 18.772	x				

[a] Coordinates are given in the WGS-84 reference system.
[b] Denotes that isotope analysis have been performed on the sample.

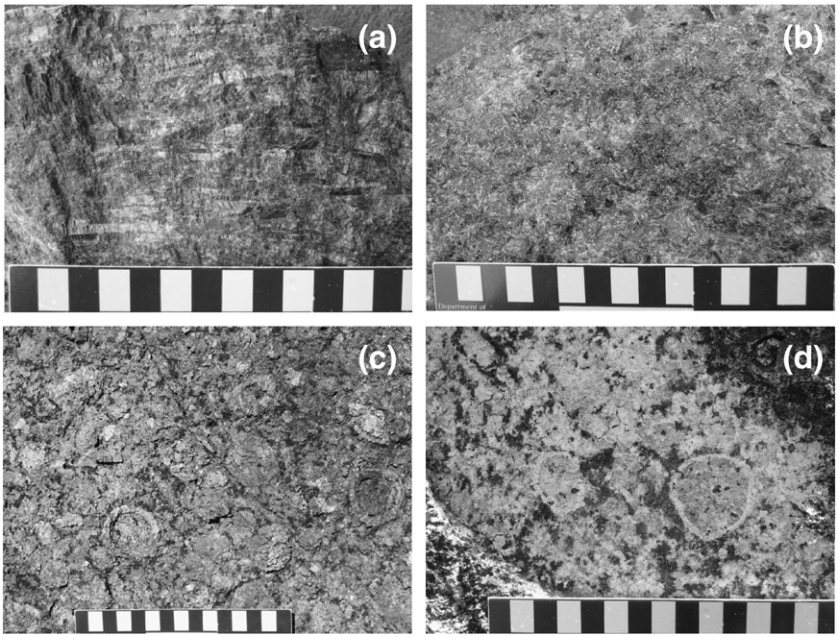

Fig. 2. Photographs of the rock types of the Mucajaí complex. (a) A strongly oriented sample of the Repartimento anorthosite (plag > 90 vol.%, with accessory pyroxenes and biotite). (b) An even-grained, homogeneous sample of a monzodiorite from the southern rim of the Repartimento anorthosite. (c) A typical sample of the Mucajaí monzonite with coarse alkali feldspar crystals that are generally not rimmed by plagioclase. (d) A sample of the main phase Mucajaí biotite–hornblende granite, with rare plagioclase rims around alkali feldspar phenocrysts.

2. Geological setting

2.1. The Mucajaí AMG complex

The ~1525 Ma Mucajaí AMG complex (Fig. 1; Fraga et al., 2009a) comprises a rapakivi granite batholith and the Repartimento anorthosite. The rapakivi batholith consists of a main phase biotite–hornblende granite (BHG) and, in its northeastern part, a more evolved biotite granite (BG). It also includes a portion of occasionally quartz-bearing fayalite-monzonitic and syenitic (FMS — fayalite mangerites and syenites of Fraga et al., 2009a) rocks that crop out in the southwestern part of the complex. Rapakivi texture of the granites is not well developed, thus the rock types of the complex are reminiscent of the pyterlitic rapakivi granite type of the *locus classicus* rapakivi suites of Finland (cf. Rämö and Haapala, 2005). The Repartimento anorthosite, which presumably intrudes the rapakivi batholith in the southwest (Fig.1a), crops out along the Repartimento River and is assumed to be in contact with the monzonitic rocks. Due to dense rain forest vegetation and poor accessibility of outcrops, contacts between the rock types have not been observed.

Based on geochemistry, Fraga et al. (2009a) considered the biotite-hornblende granite and biotite granite to be related to each other by fractional crystallization of a crustal partial melt. The monzonitic rocks are thought to have been generated independently from the main phase granites, and the anorthosite is considered to be a cumulate of a mantle-derived melt with a distinct origin from the granites.

In this study, we report monzodioritic rocks from the southern flank of the Repartimento anorthosite that have not been previously detected nor sampled because of their remote location in the rainforest. Geochemically and petrographically distinct from all the previously known rock types of the suite, the monzodioritic rocks provide new insights into the petrogenesis of the Mucajaí complex.

The Caracaraí gabbronorite (Fig. 1a) ca. 30 km southeast from the main complex has been suspected to be associated with the Repartimento anorthosite based on a biotite K–Ar age of 1664 Ma (Montalvão et al., 1975). However, this assumption still awaits confirmation as the age does not strictly correspond to the ages obtained from the Mucajaí complex and could merely reflect resetting of the K–Ar system.

Previous geochronological studies from the complex are few and varying in methods, results, and precision. Fraga et al. (2009a) presented a Pb–Pb evaporation age of 1538 ± 5 Ma for the monzonitic part of the complex. A conventional U–Pb ID–TIMS age with a relatively large uncertainty is available for the biotite granite (1544 ± 42 Ma; Gaudette et al., 1996). A SHRIMP age of 1527 ± 7 Ma was reported for the Repartimento anorthosite by Santos et al. (1999).

2.2. Country rocks

In the geochronological province model of the Amazonian craton by Tassinari and Macambira (2004), the country rocks of the magmatic suites of Parguaza, Surucucus, and Mucajaí correspond to the juvenile Transamazonian rocks of the Maroni Itacaiunas (MIP; 2.2–1.9 Ga) and the younger Ventuari–Tapajos (VTP; 1.9–1.8 Ga) provinces. These domains correspond to the Tapajos–Parima (2.03–1.88 Ga), Rio Negro (1.82–1.52 Ga), and K'Mudku (1.45–1.10 Ga) provinces of Santos et al. (2006).

In the Mucajaí region, which represents the easternmost termination of the Mesoproterozoic rapakivi belt, the country rocks comprise mostly ~1.94 Ga A-type and charnockitic granitoids, gneisses, and associated mafic rocks south of the Cauarane–Coeroene Belt (Fraga et al., 2009b). These rocks were grouped by Fraga et al. (2009b) into the Igarape Branco (allanite–biotite–hornblende granitic gneiss) and Igarape Miracelha (titanite–hornblende–biotite granitic gneiss) units (A-type granitoids) and the charnockitic Serra da Prata suite. Based on Nd isotopes, the gneisses were considered to have been generated by partial melting of juvenile Transamazonian (MIP) crustal sources (Fraga et al., 2009b).

The Mucajaí region has been affected by deformation caused by the Mesoproterozoic K'Mudku event (Cordani et al., 2010; Gibbs and Barron, 1993; Santos et al., 2006). This deformation is interpreted as a tectonic flexuring response to a collisional event in the southwestern Amazonian craton (Grenvillian-Sunsás of Santos et al., 2000). The effects of this deformation are seen in the Mucajaí complex. Mylonitization under low

to moderate temperatures caused by the K'Mudku shearing marks the southeastern border of the complex (Fraga et al., 2009a) and has also affected the already deformed country rocks (Fraga et al., 2009b).

3. Studied material

3.1. Sampling

Sample numbers, locations, rock types, and analyses performed on each sample are listed in Table 1. Sampling locations are shown in Fig. 1a.

Fraga et al. (2009a) published a detailed study on the geochemistry of the granitic and mangeritic rocks of the complex. To further characterize the rock types of the complex, four more samples were selected from the Repartimento anorthosite for geochemical analysis. In addition to these, six granitic and two new monzonitic samples were selected. Two samples from the newly discovered monzodioritic rocks are also included in the study. The geochemistry of the Caracaraí gabbronorite was tentatively compared with the main complex samples.

For isotopic studies on the age and temporal evolution of the Mucajaí complex, six representative samples of the major rock types were collected (Table 1). Four of these (anorthosite DFHR-01, quartz–fayalite monzonite DFHR-04, biotite–hornblende granite DFHR-08, and biotite granite DFHR-10) were taken from the principal rock types of the complex and two (DFHR-12 and DFHR-14) from mafic rocks outside the main complex. DFHR-12 represents the gabbronoritic intrusion of Caracaraí and DFHR-14 is a representative sample from the Paleoproterozoic mafic country rocks (Fraga et al., 2009a,b).

The two samples outside the main complex did not yield enough zircon for analysis and therefore U–Pb dating was done only on the four samples from the Mucajaí complex itself that provided abundant zircon

Table 2
Major (ICP-AES) and trace element (ICP-MS) compositions of the samples from the Mucajaí complex.

Sample number	DFHR 12	DFHR 15	DFHR 16	DFHR 22	DFHR 30 A	DFHR 30 B	DFHR 32	DFHR 03	LF 50	DFHR 07	DFHR 08	LF 09A	DFHR 09	LF 88	DFHR 18
Rock type	GBRNOR	MD	MD	ANOR	ANOR	ANOR	ANOR	MONZ	MONZ	BHG	BHG	BHG	BHG	BHG	SG
SiO_2	49.69	48.34	49.17	51.49	51.80	52.89	52.80	51.47	59.00	65.13	65.51	66.36	67.41	67.58	71.32
TiO_2	0.22	2.87	2.10	1.24	0.56	0.51	0.37	2.60	1.02	0.48	0.42	0.53	0.49	0.31	0.28
Al_2O_3	18.78	17.19	19.37	24.53	23.59	25.81	24.97	15.16	16.26	15.03	15.70	14.83	14.52	16.08	13.02
Fe_2O_3	8.01	12.67	11.50	5.07	5.42	2.62	3.45	13.07	9.49	5.84	5.09	5.54	5.18	3.08	2.17
MnO	0.12	0.16	0.13	0.06	0.14	0.04	0.07	0.18	0.16	0.10	0.08	0.10	0.09	0.05	0.03
MgO	9.62	3.32	3.92	1.39	3.57	0.80	2.07	1.99	0.67	0.25	0.22	0.25	0.29	0.11	0.28
CaO	10.79	8.85	7.96	9.95	9.45	10.31	9.67	7.19	4.29	2.75	2.68	2.31	2.16	1.81	1.45
Na_2O	1.99	3.42	3.46	3.91	3.68	4.21	4.09	3.69	3.91	3.63	3.90	3.60	3.39	3.74	3.33
K_2O	0.27	1.29	1.25	1.25	0.89	1.40	1.10	3.03	4.61	5.53	5.40	5.43	5.65	6.54	5.92
P_2O_5	0.01	0.77	0.37	0.13	0.09	0.32	0.12	1.74	0.36	0.23	0.19	0.14	0.19	0.07	0.04
LOI	0.2	0.8	0.5	0.8	0.6	0.9	1.1	−0.5	−0.2	0.7	0.5	0.6	0.3	0.4	2.0
Total	99.78	99.73	99.73	99.80	99.79	99.81	99.80	99.65	99.59	99.62	99.68	99.66	99.68	99.76	99.89
La	1.9	20.2	14.1	9.4	4.9	11.0	6.3	59.1	41.8	137.6	112.6	76.9	80.5	37.8	42.0
Ce	3.8	48.6	31.8	20.1	16.1	26.1	14.1	145.4	95.9	297.7	245.4	180.0	163.1	81.3	95.7
Pr	0.53	6.22	4.17	2.47	1.25	3.30	1.65	19.48	12.17	35.22	28.51	21.36	20.02	9.37	11.07
Nd	2.3	26.1	17.6	10.3	5.6	14.0	7.3	86.4	53.7	132.7	109.7	84.2	80.6	36.6	42.9
Sm	0.61	5.50	3.55	2.07	1.00	2.92	1.44	17.85	10.83	22.06	18.36	15.12	14.79	7.17	9.94
Eu	0.46	1.99	1.51	1.15	0.83	1.19	0.99	4.21	3.96	3.68	3.53	3.10	3.32	2.86	1.07
Gd	0.78	5.39	3.42	1.98	1.04	2.93	1.50	17.58	10.55	18.59	15.65	13.29	13.54	6.28	10.50
Tb	0.14	0.82	0.52	0.31	0.16	0.42	0.23	2.65	1.70	2.91	2.50	2.12	2.22	1.04	1.69
Dy	0.86	4.37	2.80	1.71	0.84	2.27	1.28	14.71	9.46	15.86	13.68	12.19	12.42	5.84	8.26
Ho	0.19	0.85	0.55	0.34	0.18	0.41	0.24	2.85	1.95	3.22	2.72	2.44	2.46	1.20	1.45
Er	0.57	2.35	1.57	0.94	0.49	1.17	0.67	7.81	5.72	9.20	7.81	6.95	6.90	3.35	3.78
Tm	0.09	0.34	0.21	0.14	0.07	0.16	0.09	1.08	0.84	1.37	1.17	1.06	1.05	0.51	0.56
Yb	0.64	2.01	1.31	0.91	0.48	0.97	0.58	6.59	5.44	8.74	7.60	6.81	6.80	3.30	3.33
Lu	0.10	0.29	0.20	0.13	0.07	0.14	0.08	0.94	0.85	1.31	1.13	1.04	1.00	0.50	0.46
Zr	8.4	119.0	105.3	150.8	27.3	80.5	48.5	259.9	959.7	772.2	591.3	714.6	693.5	397.5	274.1
Hf	0.3	3.4	2.7	4.0	0.6	1.8	1.2	6.4	20.9	21.0	15.9	18.2	18.4	9.3	8.6
Y	5.1	24.2	14.7	8.5	4.6	11.5	6.8	77.2	50.3	86.0	75.7	62.1	68.8	30.2	37.0
U	<0.1	1.0	0.5	0.2	<0.1	0.2	<0.1	0.7	1.4	4.9	4.5	2.9	3.2	1.5	3.0
Th	<0.2	2.9	2.2	0.5	0.2	0.6	0.4	2.0	3.5	28.9	26.2	12.0	17.1	6.4	26.0
Nb	0.2	10.0	6.6	11.0	1.5	4.3	2.8	32.1	45.8	47.9	40.4	52.8	41.0	25.9	20.3
Ta	<0.1	0.6	0.4	0.6	0.1	0.3	0.2	1.6	33.0	2.8	2.2	2.9	2.4	1.4	0.6
Ba	99	672	554	562	514	722	629	1289	1654	1246	1156	1343	1258	1390	380
Ga	16.0	20.5	21.9	20.6	18.0	19.8	18.4	24.8	24.8	26.2	26.2	24.5	23.6	24.5	17.2
Rb	2.1	30.4	20.3	14.9	5.9	16.7	9.8	47.3	87.6	194.9	182.2	170.1	199.6	181.0	284.8
Sr	176.4	448.0	511.4	707.8	655.5	743.4	728.8	319.0	236.4	150.8	159.7	147.2	145.8	148.9	74.0
Co	55.0	47.3	44.1	18.3	25.6	7.4	14.2	30.5	7.1	2.5	2.4	2.5	3.4	1.2	4.3
Sc	26	24	15	8	9	5	6	26	19	9	8	11	8	4	8
V	92	240	241	77	72	26	31	123	9	<8	<8	<8	<8	<8	25
Cu	121.6	25.6	68.1	25.5	7.7	10.9	15.2	32.5	6.7	8.4	5.5	6.8	6.0	2.1	1.7
Mo	<0.1	0.6	0.4	0.3	<0.1	0.2	<0.1	1.9	1.5	2.5	2.2	1.3	0.7	0.4	0.8
Ni	174.3	11.0	47.0	28.6	35.2	7.4	21.7	11.3	1.4	0.6	0.5	6.0	0.6	6.0	3.6
Pb	0.9	1.3	1.2	0.6	0.8	0.5	0.3	1.1	1.3	29.7	27.7	16.9	15.6	16.2	17.5
Zn	5	43	30	19	16	10	12	51	94	88	79	88	70	43	32
Eu/Eu*	2.0	1.1	1.3	1.7	2.5	1.2	2.1	0.7	1.1	0.6	0.6	0.7	0.7	1.3	0.3
$(La/Yb)_N$	2.0	6.8	7.3	7.0	6.9	7.7	7.4	6.1	5.2	11	10	7.7	8.0	7.8	8.6

Abbreviations: ANOR—anorthosite, BG—biotite granite, BHG—biotite–hornblende granite, GBRNOR—gabbronorite, MD—monzodiorite, MONZ—monzonite, SG—syenogranite.
Major elements are quoted in wt.%, trace-elements in ppm.
Eu/Eu* = EuN/[(SmN × GdN)-1] and (La/Yb)N normalized to chondritic values of Sun and McDonough (1989).
Cr_2O_3, Be, Cs, Ni, Sn, W, Ag, As, Au, Bi, Cd, Hg, Sb, Se, and Tl were also analyzed but their levels generally fell below detection limits so they were omitted from the table. Analytical files are available upon request from the authors.

for ID–TIMS work. Whole-rock Sm–Nd analyses were performed on all six samples. Zircon O and Lu–Hf isotope data were acquired from the same samples and fractions used in U–Pb geochronology.

3.2. Petrography

The anorthosites (Fig. 2a) consist mainly (>90 vol.%) of subhedral, locally deformed and antiperthitic plagioclase (An_{58-48}) megacrysts (5 to 20 cm long) with minor interstitial orthopyroxene, clinopyroxene, and rare relict olivine.

The monzodiorites (Fig. 2b) are coarse-grained equigranular rocks with subhedral and oriented tabular, commonly antiperthitic, plagioclase (An_{50-30}) and interstitial, ortho- and clinopyroxene as the main minerals. Mutual quantities of the pyroxenes vary and they are commonly intergrown and occasionally also with feldspars. Interstitial microperthitic alkali feldspar is present and apatite is the most important accessory mineral. Some secondary amphibole, carbonates and chlorite are also present.

The quartz–fayalite monzonites and syenites (FMS series of Fraga et al., 2009a; Fig. 2c) are porphyritic rocks with locally plagioclase mantled alkali feldspar and subordinate plagioclase phenocrysts set in a medium- to coarse-grained groundmass composed of alkali feldspar, plagioclase, and anhedral orthopyroxene with minor clinopyroxene and fayalite. Porphyritic types with spherical alkali feldspar megacrysts up to 7 cm have also been observed.

The main phase biotite–hornblende granites (BHG; Fig. 2d) of the complex are porphyritic rapakivi granites and consist of spherical alkali feldspar phenocrysts (up to 12 cm in diameter) in a coarse-grained groundmass of alkali feldspar, quartz, plagioclase, and irregular aggregates of anhedral, interstitial green hornblende and minor brown biotite. Accessory minerals include apatite, zircon, ilmenite>magnetite, and minor amounts of allanite, fluorite, and titanite.

The more evolved biotite granites (BG) are petrographically similar to the biotite–hornblende granites with the exception of biotite being the main and hornblende the subordinate mafic mineral. They are porphyritic rocks with dominant tabular alkali feldspar megacrysts and,

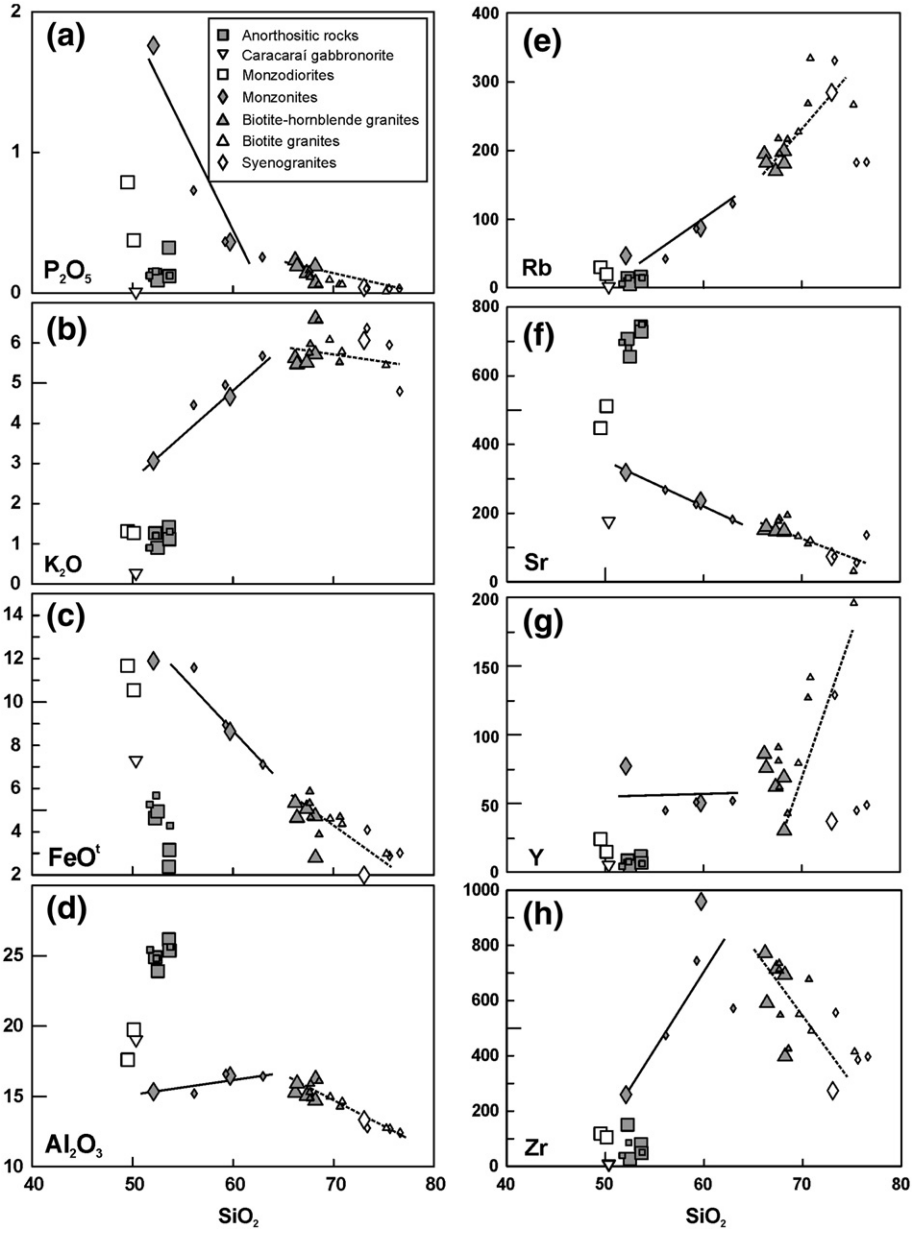

Fig. 3. Selected major- (in wt.% oxides) and trace-element (in ppm) diagrams showing the samples from the Mucajaí complex and Caracaraí gabbronorite. Large symbols denote new data, small symbols denote analysis from Fraga et al. (2009a). Linear visual best-fit trends are also shown for the monzonitic (continuous line) and granitic (dashed line) rocks.

compared to the main phase granite, characterized by a more evolved accessory mineral composition dominated by allanite and fluorite.

4. Analytical methods

For elemental geochemistry 6 to 12 kg of sample material was crushed and milled in a ceramic disk grinder at the Laboratory of Mineral Analyses of the Geological Survey of Brazil (CPRM). For isotope analysis the whole-rock samples were jaw-crushed in a Mn steel crusher and heavy mineral fractions were separated with heavy liquids and a Franz magnetic separator at the Research Laboratory of the Geological Survey of Finland.

Major and trace element analyses were done at the Acme Analytical Laboratories Ltd., Canada. The U–Pb and Sm–Nd ID–TIMS analyses were performed at the Research Laboratory of the Geological Survey of Finland, oxygen isotope SIMS analysis at the NordSIMS facility of the Swedish Museum of Natural History in Stockholm, Sweden and the LAM-ICP-MS Hf isotope analysis at the Department of Geosciences, University of Oslo, Norway.

4.1. Elemental geochemistry

ICP-AES after lithium borate fusion was used to determine the major element concentrations. ICP-MS was used on the trace elements with Ba, Co, Ga, Rb, Sr, Th, V, Y, Zr, REE and the incompatible elements from lithium borate fusion and Cu, Pb, and Zn after aqua regia digestion.

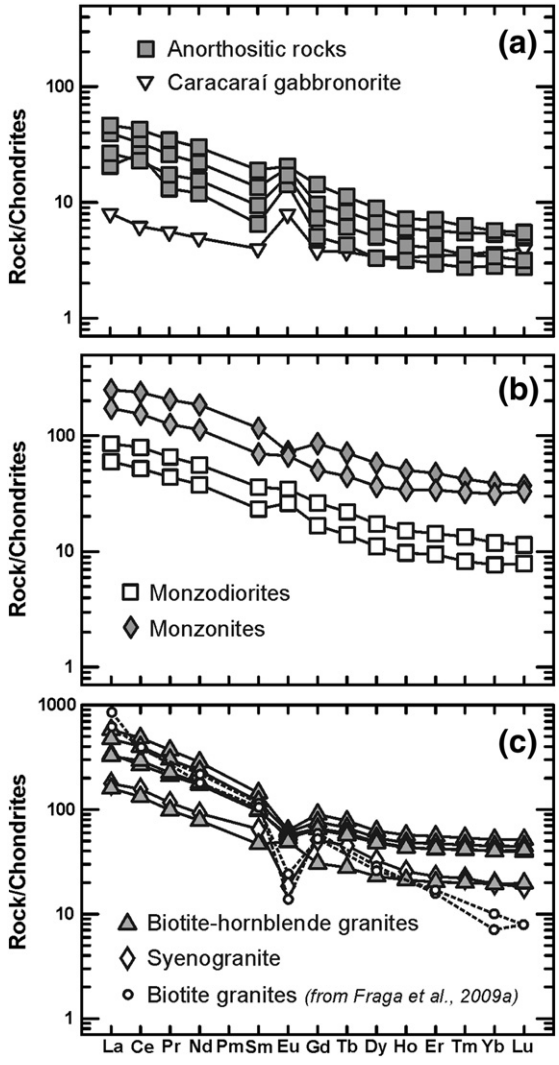

Fig. 4. Chondrite normalized (Sun and McDonough, 1989) REE diagrams of the Mucajaí and Caracaraí samples. Data for the biotite granites is from Fraga et al. (2009a).

4.2. Zircon U–Pb geochronology

Heavy mineral fractions were carefully handpicked to extract the non-fractured, transparent, and inclusion-free zircon crystals for U–Pb analysis. In the coarser fractions, where intact crystals were not present, fragments with certain magmatic morphology were picked. To enhance the concordance of the analyses, the samples were air-abraded in a pneumatic abrasion mill.

The decomposition of zircon and extraction of U and Pb for multigrain ID–TIMS (isotopic dilution–thermal ionization mass spectrometry) isotopic age determinations followed mainly the procedure of Krogh (1973, 1982). ^{235}U–^{208}Pb-spiked and unspiked isotopic ratios were measured using a VG Sector 54 thermal ionization multicollector mass spectrometer in static mode. According to repeated measurements of the NBS981 Pb standard, the measured lead isotope ratios were corrected for 0.12–0.10 per a.m.u. fractionation (assuming uncertainty of ±0.07%). PbDat- (Ludwig, 1991) and Isoplot/Ex 3- (Ludwig, 2003) programs were used to calculate and plot the U–Pb data. Age errors are calculated at 2σ and decay constant errors ignored. Data-point error ellipses in all figures are 2σ.

4.3. Whole-rock Sm–Nd isotopes

Whole-rock powders (~180 mg) were dissolved with a total ^{149}Sm–^{150}Nd tracer spike for a minimum of 2 days in a teflon bomb at 180 °C in HF-HNO_3. After evaporation, the samples were dissolved in HCl to obtain clear solutions. REE were separated using standard cation exhange chromatography and Sm and Nd were purified using a modified version of the Teflon-HDEHP method of Richard et al. (1976). The total procedural blank was <300 pg for Nd.

Isotope ratios of Sm and Nd were measured in dynamic mode on a VG SECTOR 54 mass spectrometer. Nd isotope ratios were normalized to $^{146}Nd/^{144}Nd = 0.7219$. Based on repeated analysis of the La Jolla Nd standard the external 2σ error on $^{143}Nd/^{144}Nd$ is estimated at ~0.0025% and the Sm–Nd ratios are estimated to be accurate within 0.5%. The maximum error in the calculated ε_{Nd} values is ±0.4 ε units. Decay constant of 6.54×10^{-12} a^{-1} for ^{147}Sm, depleted mantle model of DePaolo (1981), and the model for CHUR of DePaolo and Wasserburg (1976) were used.

4.4. Zircon O isotopes

Zircons for in situ oxygen isotope analysis were picked from suitable heavy mineral fractions that provided concordant U–Pb ID–TIMS age results. The samples were mounted in epoxy together with standard in the central 12 mm area of the sample, sectioned approximately in half, polished to surface, and Au-coated. SEM imaging was performed prior to coating to avoid targeting unsuitable crystals in the analysis.

Zircon oxygen isotopes were measured by a Cameca IMS1280 multicollector ion microprobe. The instrument setup and analytical procedures followed closely those of Whitehouse and Nemchin (2009), utilizing a ca. 2 nA Cs^+ primary ion beam together with a normal incidence low energy electron gun for charge compensation, medium field magnification (ca. 80×) and two Faraday detectors (channels L'2 and H'2) at a common mass resolution of ~2500. Measurements were performed in pre-programmed chain analysis mode with automatic field aperture and entrance slit centering on the ^{16}O signal. The magnetic field was locked using NMR regulation for the entire analytical session. Each data-acquisition run comprised a 20 × 20 μm pre-sputter to remove Au layer followed by the centering steps and 64 s of data integration performed using a non-rastered, ca.

Table 3
U–Pb zircon data for the samples of the Mucajaí complex.

Sample and analyzed zircon fractions	Conc (ppm)		Measured	Radiogenic	Isotope ratios[a]				Apparent ages		
	U	Pb	$^{206}Pb/^{204}Pb$	$^{208}Pb/^{206}Pb$	$^{206}Pb/^{238}U$	$^{207}Pb/^{235}U$	$^{207}Pb/^{206}Pb$	Rho[b]	$^{206}Pb/^{238}U$	$^{207}Pb/^{235}U$	$^{207}Pb/^{206}Pb$
DFHR-01, Repartimento anorthosite											
A) Brown, d>4.2, abr. 24 h	403	121	536712	0.21	0.2662 ± 0.53	3.487 ± 0.53	0.0950 ± 0.07	0.99	1522	1524	1528 ± 1.4
B) Colorless, d>4.2, abr. 24 h	287	87	105544	0.23	0.2661 ± 0.53	3.481 ± 0.53	0.0949 ± 0.07	0.99	1521	1523	1526 ± 1.4
DFHR-04, Mucajaí monzonite											
A) Colorless, d>4.2, abr. 5 h	71	20	35881	0.15	0.2661 ± 0.57	3.483 ± 0.57	0.0949 ± 0.15	0.97	1521	1523	1527 ± 2.7
B) Colorless, d>4.2, abr. 16 h	61	17	78956	0.15	0.2654 ± 0.54	3.476 ± 0.55	0.0949 ± 0.09	0.99	1517	1522	1528 ± 1.6
DFHR-08, Mucajaí biotite-hornblende granite											
A) Colorless, d>4.2, g>150 μm abr. 24 h	134	37	9950	0.12	0.2653 ± 0.53	3.476 ± 0.53	0.0950 ± 0.07	0.99	1517	1522	1529 ± 1.4
B) Colorless, d>4.2, g<150 μm abr. 24 h	133	38	13474	0.14	0.2659 ± 0.53	3.483 ± 0.54	0.0950 ± 0.07	0.99	1520	1523	1528 ± 1.4
DFHR-10, Mucajaí biotite granite											
A) Colorless, d>4.2, g>75 μm abr. 24 h	148	42	4391	0.14	0.2647 ± 0.55	3.451 ± 0.56	0.0946 ± 0.08	0.99	1514	1516	1520 ± 1.5
B) Colorless, d>4.2, g<75 μm abr. 24 h	330	91	21324	0.13	0.2628 ± 0.56	3.431 ± 0.56	0.0947 ± 0.07	0.99	1504	1512	1522 ± 1.4
C) Brown, d>4.2, g<75 μm abr. 24 h	1730	458	5188	0.11	0.2524 ± 0.53	3.300 ± 0.54	0.0948 ± 0.07	0.99	1451	1481	1524 ± 1.4
D) Colorless, d>4.2, g<75 μm abr. 24 h	152	42	6208	0.13	0.2570 ± 0.63	3.364 ± 0.64	0.0949 ± 0.08	0.99	1475	1496	1527 ± 1.5
E) Colorless, d>4.2, g<75 μm abr. 24 h	169	47	12183	0.13	0.2640 ± 0.53	3.445 ± 0.54	0.0947 ± 0.08	0.99	1510	1515	1521 ± 1.5

Abbreviations: abr = abrasion time, d = specific gravity (g/cm^3), g = grain size (if no grain size is indicated, the whole weight fraction was used to pick the grains).
All errors are 2σ.
[a] Isotopic ratios corrected for fractionation (0.1–0.12/a.m.u.), blank (10 pg), and age related common lead (Stacey and Kramers, 1975; $^{206}Pb/^{204}Pb \pm 0.2$, $^{207}Pb/^{204}Pb \pm 0.1$, $^{208}Pb/^{204}Pb \pm 0.2$).
[b] Rho: calculated error correlation between $^{206}Pb/^{238}U$ and $^{207}Pb/^{235}U$ ratios.

10 μm spot. Field aperture centering values reported in Appendix A are well within those for which no bias has been observed during tests on standard mounts (Whitehouse and Nemchin, 2009). A total of 81 unknowns (~20/sample) were measured during three analysis sessions. In the measurement chain, every set of four unknowns was followed by two bracketing analyses on the Geostandards 91500 zircon. A $\delta^{18}O$ value of +9.86‰ (SMOW, Wiedenbeck et al., 2004) was assumed for the 91500 zircon in data normalization and small linear-drift corrections were applied to each session. External reproducibility of ±0.17 to 0.29‰ (1SD; Appendix A) based on the

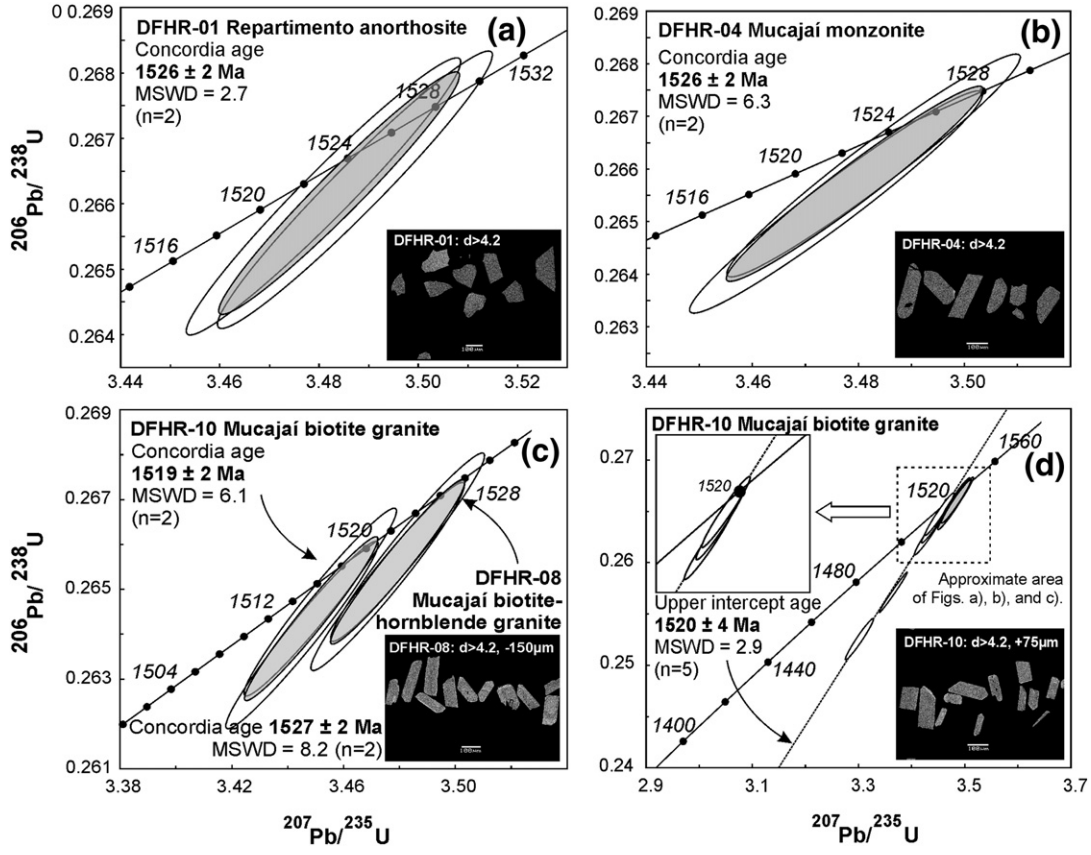

Fig. 5. Concordia diagrams with best estimates for the crystallization ages of the rock types of the Mucajaí complex. (a) Repartimento anorthosite (DFHR-01). (b) Mucajaí monzonite (DFHR-04). (c) Concordant fractions of the Mucajaí rapakivi granites (DFHR-08 and DFHR-10). (d) All U–Pb analyses from the Mucajaí complex rocks and the discordia line for the Mucajaí biotite granite (DFHR-10). Insets show BSE images of the respective zircon fractions used in the TIMS analysis.

Table 4
Whole-rock Sm–Nd isotope data for the rocks of the Mucajaí complex.

Sample	Rock type	Sm (ppm)	Nd (ppm)	$^{147}Sm/^{144}Nd$	$^{143}Nd/^{144}Nd_{(0)}$	$^{143}Nd/^{144}Nd_{(t)}$	$\varepsilon_{Nd(t)}$	t (Ma)	$T_{(DM)}$ (Ma)
Mucajaí complex									
DFHR-01	Anorthosite	2.39	12.06	0.1197	0.511771 ± 5	0.510571	−1.9	1525	2059
DFHR-04	Quartz–fayalite monzonite	12.83	59.75	0.1298	0.511853 ± 10	0.510552	−2.3	1525	2159
DFHR-08	Biotite–hornblende granite	12.78	78.51	0.0984	0.511550 ± 5	0.510563	−2.0	1525	1969
DFHR-10	Biotite granite	22.93	134.76	0.1029	0.511558 ± 5	0.510527	−2.8	1525	2038
Caracaraí									
DFHR-12	Gabbronorite	0.49	1.66	0.1802	0.512514 ± 5	0.510708	0.8	1525	2429
Country rock									
DFHR-14	Gabbronorite	3.65	14.51	0.1523	0.512174 ± 5	0.510229	2.0	1940	2157

Note: initial isotope ratios are calculated at t, which denotes the average age of the Mucajaí complex at 1525 Ma (except for sample DFHR-14 where t = 1940).

standard measurements was propagated onto the overall uncertainty for each analysis. Analytical file with further details is available in electronic form in Appendix A.

4.5. Zircon Lu–Hf isotopes

Hf isotopes were measured from the same sample mounts after the (less destructive) oxygen analysis. The laser ablation for Hf analysis was done after the topmost layer and gold coating was removed by light re-polishing of the mounts.

Hf isotope compositions of the zircons were analyzed by laser-ablation multicollector inductively coupled plasma source mass spectrometry (LAM-ICP-MS) using a Nu Plasma HR mass spectrometer and a NewWave LUV213 laser microprobe. The analytical protocols including an empirical correction for isobaric interferences on ^{176}Hf are described in detail in Heinonen et al. (2010a). The laser spot size was 55 μm. Mud Tank and Temora-2 zircon standards were run in frequent intervals as unknowns (present-day $^{176}Hf/^{177}Hf$ of 0.282509 ± 44, n = 831; 0.282679 ± 61, n = 460 respectively). The observed external reproducibility on the Temora-2 reference material gives an uncertainty estimate of ±2 epsilon units on single in situ analysis. In all calculations we have adopted the decay constant of 1.867×10^{-11} a^{-1} for ^{176}Lu (Scherer et al., 2001, 2007; Söderlund et al., 2004), present-day chondritic composition of $^{176}Hf/^{177}Hf = 0.282785$ and $^{176}Lu/^{177}Hf = 0.0336$ (Bouvier et al., 2008) and the depleted mantle model of Griffin et al. (2000) modified to agree with the CHUR parameters and decay constant used.

5. Results

5.1. Major and trace element geochemistry

Geochemical compositions of the studied rocks are given in Table 2 and plotted on variation diagrams in Fig. 3 and on REE diagrams in Fig. 4. Geochemical data from Fraga et al. (2009a) are included in Fig. 3 and Discussion.

Major and trace element compositions of the anorthositic rocks are evidently controlled by cumulus plagioclase (Fig. 3). The monzonitic rocks plot on well-defined compositional trends from SiO_2 51 to 62 wt.% (Fig. 3). If interpreted as fractionation trends, they show a broad increase in K_2O, Al_2O_3, Rb, and especially Zr as SiO_2 increases. Negatively correlated trends with SiO_2 of P_2O_5, FeO_t, and Sr indicate apatite, oxides, and plagioclase as likely fractionating phases controlling the composition of the liquid. No clear trend in REE evolution of the monzonitic rocks is observed though (e.g., SiO_2 vs. Y, Fig. 3g). The granitic rocks form less well-defined trends from SiO_2 ~66 to ~76 wt.% with the biotite–hornblende granites with lowest SiO_2 and biotite granite and syenogranites in the higher end. The granitic trends are clearly distinct from the ones defined by the

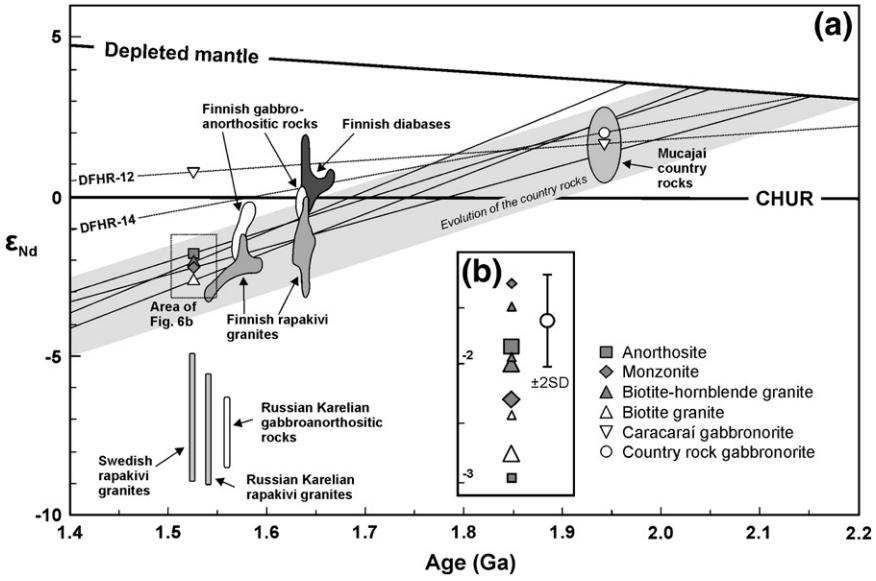

Fig. 6. Age vs. initial ε_{Nd} diagram of the studied samples shown with CHUR (Chondritic Uniform Reservoir; DePaolo and Wasserburg, 1976) and DM (Depleted mantle; DePaolo, 1981) models. Nd isotope composition and evolution of the Mucajaí country rocks are from Fraga et al. (2009a). Nd isotope compositions of the 1650–1540 Ma Finnish (Rämö, 1991), 1560–1540 Ma Russian Karelian (Neymark et al., 1994; Rämö, 1991), and 1520 Ma Swedish (Andersson et al., 2001) rapakivi granites and associated rocks are also shown for comparison. (b) Enlarged area of the diagram showing analysis of similar rocks from Fraga et al. (2009a) with small symbols.

Table 5
Zircon Lu–Hf and O isotope results for the Mucajaí samples.

Spot	$\delta^{18}O$	± 1SE	$^{176}Hf/^{177}Hf$	±2SE	$^{178}Hf/^{177}Hf$	±2SE	$^{176}Lu/^{177}Hf$	±2SE	$^{176}Yb/^{177}Hf$	±2SE	$^{176}Hf/^{177}Hf(t)$	±2SE	εHf(t)	±2SE
DFHR-01, Repartimento anorthosite, T = 1526 Ma														
01	6.97	0.21	0.281797	0.000019	1.46726	0.00006	0.000991	0.000001	0.0433	0.0010	0.281768	0.000019	−1.6	0.7
02	6.86	0.22	0.281772	0.000022	1.46733	0.00006	0.000746	0.000003	0.0333	0.0010	0.281750	0.000022	−2.3	0.8
03	7.55	0.20	0.281761	0.000020	1.46716	0.00006	0.000329	0.000005	0.0138	0.0006	0.281751	0.000020	−2.2	0.7
04a	6.84	0.21	0.281715	0.000036	1.46712	0.00009	0.000589	0.000040	0.0173	0.0004	0.281698	0.000036	−4.1	1.2
04b	7.36	0.20												
05a	7.25	0.25	0.281708	0.000046	1.46722	0.00011	0.000450	0.000064	0.01556	0.0009	0.281695	0.000046	−4.2	1.6
05b	7.41	0.21												
06	7.10	0.21	0.281791	0.000034	1.46721	0.00011	0.000528	0.000078	0.0172	0.0011	0.281776	0.000034	−1.4	1.1
07	6.68	0.23	0.281763	0.000032	1.46724	0.00010	0.001205	0.000128	0.0438	0.0013	0.281728	0.000032	−3.0	1.0
08	6.34	0.23	0.281708	0.000028	1.46719	0.00006	0.000514	0.000056	0.0203	0.0019	0.281693	0.000028	−4.3	0.9
09	6.22	0.35	0.281814	0.000024	1.46716	0.00005	0.000802	0.000024	0.0355	0.0003	0.281791	0.000024	−0.8	0.8
10	6.52	0.27	0.281761	0.000032	1.46724	0.00006	0.000941	0.000005	0.0425	0.0011	0.281734	0.000032	−2.8	1.1
11	6.13	0.26	0.281763	0.000026	1.46729	0.00005	0.000795	0.000005	0.0362	0.0009	0.281740	0.000026	−2.6	0.9
12	6.68	0.32	0.281760	0.000026	1.46719	0.00005	0.000433	0.000036	0.0193	0.0022	0.281747	0.000026	−2.4	0.9
13	6.97	0.30												
14	6.34	0.36	0.281792	0.000024	1.46720	0.00006	0.000758	0.000100	0.0221	0.0019	0.281770	0.000024	−1.6	0.7
15	6.35	0.34	0.281799	0.000020	1.46728	0.00007	0.000775	0.000026	0.0336	0.0009	0.281777	0.000020	−1.3	0.7
16	5.90	0.33	0.281908	0.000034	1.46727	0.00011	0.002046	0.000028	0.0993	0.0016	0.281849	0.000034	1.2	1.2
17	6.45	0.31	0.281769	0.000050	1.46723	0.00012	0.000801	0.000116	0.0274	0.0016	0.281746	0.000050	−2.4	1.7
18	6.32	0.33	0.281773	0.000022	1.46724	0.00008	0.000635	0.000008	0.0280	0.0011	0.281755	0.000022	−2.1	0.8
19			0.281779	0.000019	1.46715	0.00005	0.000688	0.000004	0.0308	0.0007	0.281759	0.000019	−1.9	0.7
20			0.281721	0.000026	1.46730	0.00007	0.000344	0.000040	0.0157	0.0015	0.281711	0.000026	−3.7	0.9
21			0.281804	0.000022	1.46723	0.00008	0.000549	0.000016	0.0246	0.0016	0.281788	0.000022	−0.9	0.8
22			0.281777	0.000028	1.46715	0.00006	0.000976	0.000054	0.0412	0.0016	0.281749	0.000028	−2.3	0.9
DFHR-04, Mucajaí monzonite, T = 1526 Ma														
01	7.68	0.25	0.281752	0.000022	1.46714	0.00007	0.000381	0.000004	0.0158	0.0004	0.281741	0.000022	−2.6	0.8
02	7.44	0.24	0.281783	0.000022	1.46718	0.00005	0.000665	0.000010	0.0293	0.0010	0.281764	0.000022	−1.8	0.8
03	7.95	0.21	0.281760	0.000028	1.46719	0.00011	0.000902	0.000118	0.0434	0.0066	0.281734	0.000028	−2.8	0.9
04	7.41	0.19	0.281752	0.000032	1.46728	0.00007	0.000879	0.000020	0.0408	0.0015	0.281727	0.000032	−3.1	1.1
05a	7.29	0.21	0.281755	0.000024	1.46727	0.00006	0.000292	0.000003	0.0124	0.0002	0.281747	0.000024	−2.4	0.8
05b	7.20	0.23												
06a	7.49	0.20	0.281741	0.000019	1.46721	0.00006	0.000531	0.000044	0.0228	0.0017	0.281726	0.000019	−3.1	0.6
06b	6.85	0.23												
07	7.65	0.23	0.281765	0.000024	1.46710	0.00006	0.000375	0.000003	0.0157	0.0006	0.281754	0.000024	−2.1	0.8
08	7.03	0.25												
09	5.98	0.29	0.281706	0.000024	1.46730	0.00006	0.000353	0.000004	0.0150	0.0003	0.281696	0.000024	−4.2	0.8
10	6.78	0.32												
11	6.20	0.28	0.281738	0.000022	1.46720	0.00005	0.000560	0.000017	0.0245	0.0016	0.281722	0.000022	−3.3	0.8
12	6.61	0.30												
13	7.49	0.28	0.281774	0.000022	1.46715	0.00005	0.000783	0.000050	0.0348	0.0016	0.281751	0.000022	−2.2	0.7
14	6.75	0.31	0.281802	0.000040	1.46718	0.00009	0.000529	0.000028	0.0232	0.0004	0.281787	0.000040	−1.0	1.4
15	6.97	0.35	0.281706	0.000024	1.46727	0.00007	0.000809	0.000046	0.0363	0.0032	0.281683	0.000024	−4.7	0.8
16	7.27	0.33	0.281734	0.000022	1.46725	0.00004	0.000382	0.000008	0.0162	0.0004	0.281723	0.000022	−3.2	0.8
17	7.22	0.32	0.281738	0.000026	1.46718	0.00006	0.000370	0.000010	0.0161	0.0003	0.281727	0.000026	−3.1	0.9
18	6.99	0.31												
19			0.281736	0.000020	1.46719	0.00005	0.000325	0.000009	0.0139	0.0003	0.281727	0.000020	−3.1	0.7
20			0.281723	0.000022	1.46733	0.00007	0.000473	0.000005	0.0209	0.0007	0.281709	0.000022	−3.7	0.8
DFHR-08, Mucajaí hornblende-biotite granite, T = 1527 Ma														
01	6.62	0.24												
02	7.29	0.25	0.281773	0.000020	1.46732	0.00007	0.001458	0.000116	0.0660	0.0090	0.281731	0.000020	−2.9	0.6
03	7.05	0.21	0.281713	0.000024	1.46739	0.00006	0.000618	0.000088	0.0271	0.0020	0.281695	0.000024	−4.2	0.8
04a	7.21	0.23												
04b	6.68	0.21												
05a	7.09	0.22	0.281783	0.000022	1.46730	0.00007	0.000966	0.000032	0.0449	0.0028	0.281755	0.000022	−2.1	0.7
05b	7.09	0.22												
06	7.25	0.20	0.281760	0.000022	1.46729	0.00007	0.000800	0.000114	0.0359	0.0054	0.281737	0.000022	−2.7	0.7
07	6.87	0.24	0.281766	0.000024	1.46725	0.00007	0.000935	0.000042	0.0441	0.0020	0.281739	0.000024	−2.6	0.8
08	6.88	0.24	0.281729	0.000017	1.46734	0.00005	0.000683	0.000015	0.0310	0.0005	0.281709	0.000017	−3.7	0.6
09	6.40	0.31	0.281753	0.000028	1.46730	0.00008	0.000773	0.000030	0.0376	0.0022	0.281731	0.000028	−2.9	1.0
10a	6.36	0.35	0.281709	0.000022	1.46727	0.00007	0.000773	0.000019	0.0355	0.0011	0.281687	0.000022	−4.5	0.8
10b	6.25	0.31	0.281683	0.000020	1.46740	0.00007	0.000562	0.000013	0.0254	0.0001	0.281667	0.000020	−5.2	0.7
11	6.26	0.29	0.281772	0.000024	1.46733	0.00006	0.000924	0.000012	0.0428	0.0013	0.281745	0.000024	−2.4	0.8
12	6.84	0.33	0.281793	0.000026	1.46725	0.00006	0.000943	0.000048	0.0429	0.0018	0.281766	0.000026	−1.7	0.9
13	7.01	0.34	0.281765	0.000026	1.46730	0.00005	0.000464	0.000009	0.0203	0.0010	0.281752	0.000026	−2.2	0.9
14	6.76	0.31	0.281758	0.000022	1.46728	0.00005	0.000829	0.000090	0.0361	0.0032	0.281734	0.000022	−2.8	0.7
15	7.49	0.31	0.281751	0.000022	1.46730	0.00005	0.000809	0.000080	0.0362	0.0030	0.281728	0.000022	−3.0	0.7
16	7.06	0.31	0.281744	0.000020	1.46729	0.00005	0.000918	0.000032	0.0413	0.0016	0.281717	0.000020	−3.4	0.7
17	6.75	0.32												
18			0.281754	0.000022	1.46728	0.00005	0.000736	0.000022	0.0325	0.0020	0.281733	0.000022	−2.9	0.8
19			0.281725	0.000024	1.46741	0.00005	0.000800	0.000034	0.0367	0.0011	0.281702	0.000024	−4.0	0.8

(continued on next page)

Table 5 (*continued*)

Spot	$\delta^{18}O$	± 1SE	$^{176}Hf/^{177}Hf$	±2SE	$^{178}Hf/^{177}Hf$	±2SE	$^{176}Lu/^{177}Hf$	±2SE	$^{176}Yb/^{177}Hf$	±2SE	$^{176}Hf/^{177}Hf(t)$	±2SE	εHf(t)	±2SE
DFHR-10, Mucajaí biotite granite, T = 1519 Ma														
01	6.05	0.24	0.281785	0.000028	1.46715	0.00005	0.000786	0.000016	0.0358	0.0013	0.281762	0.000028	−2.0	1.0
02	6.33	0.23	0.281765	0.000022	1.46729	0.00006	0.000858	0.000036	0.0385	0.0015	0.281740	0.000022	−2.8	0.7
02b			0.281743	0.000020	1.46721	0.00006	0.000458	0.000012	0.0200	0.0003	0.281730	0.000020	−3.1	0.7
03	6.72	0.26												
04	6.11	0.22	0.281802	0.000028	1.46720	0.00006	0.000899	0.000044	0.0404	0.0024	0.281776	0.000028	−1.5	0.9
04b			0.281746	0.000020	1.46727	0.00007	0.000705	0.000074	0.0309	0.0016	0.281726	0.000020	−3.3	0.6
05	6.42	0.22												
06	5.95	0.26	0.281843	0.000036	1.46724	0.00007	0.001105	0.000006	0.0525	0.0019	0.281811	0.000036	−0.2	1.3
07	6.33	0.25												
08a	6.23	0.27	0.281781	0.000024	1.46722	0.00007	0.000653	0.000090	0.0291	0.0054	0.281762	0.000024	−2.0	0.8
08b	5.80	0.24												
08c			0.281753	0.000026	1.46728	0.00007	0.000763	0.000106	0.0351	0.0060	0.281731	0.000026	−3.1	0.8
09	5.95	0.24	0.281880	0.000026	1.46727	0.00009	0.002810	0.000026	0.1013	0.0040	0.281799	0.000026	−0.7	0.9
10a	5.97	0.29												
10b	5.43	0.36												
11	5.62	0.28	0.281780	0.000030	1.46730	0.00008	0.001328	0.000086	0.0428	0.0019	0.281742	0.000030	−2.7	1.0
12	5.89	0.28												
13	6.21	0.35												
14	6.03	0.33												
15	6.06	0.32												
16	6.12	0.35	0.281837	0.000036	1.46734	0.00014	0.001316	0.000070	0.0577	0.0016	0.281799	0.000036	−0.7	1.2
17a	6.02	0.32												
17b	6.49	0.33												

monzonitic rocks. This indicates either an abrupt change in fractionating phases in the magmatic lineage or, as Fraga et al. (2009a) suggested, a different origin for the rock types. The Caracaraí gabbronorite does not show clear geochemical affinity to neither the anorthositic nor the monzodioritic rocks.

The anorthositic rocks have the least enriched REE patterns of the rock types (Fig. 4a) with moderate positive Eu anomalies (Eu/Eu* from 1.2 to 2.5). The two monzodiorites have slightly more enriched REE patterns (Fig. 4b) without significant Eu anomalies (Eu/Eu* 1.1 and 1.3). The monzonites have REE patterns (Fig. 4b) comparable to the biotite–hornblende granites (Fig. 4c). Both have either negligible or slightly negative Eu anomalies (Eu/Eu* from 0.6 to 1.1), except for one granite sample (LF-88), which is clearly less REE enriched and has a small positive Eu anomaly (Eu/Eu* ~1.3). The syenogranite (DFHR-18) has a similar REE pattern (Fig. 4c) to the biotite–hornblende granites but a fairly strong negative Eu anomaly (Eu/Eu* ~0.3). The Caracaraí gabbronorite (DFHR-12) seems to have a distinctively flatter and less enriched REE pattern (Fig. 4a) than any of the other rock types. Two biotite granite samples analyzed by Fraga et al. (2009a) show that the Mucajaí biotite granite has a more fractionated REE pattern illustrated by relatively higher LREE and respectively lower HREE abundances (Fig. 4c).

5.2. U–Pb geochronology

Geochronological results are given in Table 3 and illustrated on concordia diagrams in Fig. 5.

Zircon grains analyzed from the Repartimento anorthosite (DFHR-01) are brownish to colorless, clear, and inclusion-free fragments of originally bigger crystals (Fig. 5a inset). The two analyzed fractions are concordant (Fig. 5a) with overlapping $^{207}Pb/^{206}Pb$ ages (1528 ± 2 Ma and 1526 ± 2 Ma). The mean concordia age of 1526 ± 2 Ma (MSWD = 2.7) is interpreted to be the best estimate for the crystallization age of the anorthosite.

Two fractions of euhedral, colorless, clear and inclusion-free zircons (Fig. 5b inset) were analyzed from the quartz-fayalite monzonite (DFHR-04). The almost identical and concordant U-Pb data (Fig. 5b) yield a mean concordia age of 1526 ± 2 Ma for the crystallization of the monzonite. Even though the MSWD is high (6.3), this age estimate is considered robust on the grounds of the overlapping $^{207}Pb/^{206}Pb$ ages (1527 ± 3 Ma and 1528 ± 2 Ma) of both fractions.

Two clear, inclusion-free, colorless and euhedral zircon fractions (Fig. 5c inset) were analyzed from the biotite–hornblende granite (DFHR-08). A concordant mean age of 1527 ± 2 Ma (Fig. 5c) is comparable to the mean of the $^{207}Pb/^{206}Pb$ ages (1529 ± 2 Ma and 1528 ± 2 Ma) despite the potential uncertainty inherent in the high MSWD (8.2). We consider this a good estimate of the crystallization age of the biotite–hornblende granite.

Most of the zircons from the biotite granite (DFHR-10) are fractured, rich in inclusions, turbid, and brown. Five fractions of clear prismatic crystals (Fig. 5d inset) were picked for analysis. Two of the analyses provide a concordia age of 1519 ± 2 Ma (Fig. 5c), which is identical to the upper intercept of the five-point discordia (1520 ± 4 Ma; Fig. 5d). The concordia age, as for the other samples, is preferred as the crystallization age for the biotite granite.

5.3. Sm–Nd isotopes

The whole-rock Nd isotope compositions of the studied samples are given in Table 4 and illustrated on an age vs. ε_{Nd} diagram in Fig. 6.

The $^{147}Sm/^{144}Nd$ ratios of the Mucajaí complex rocks vary from 0.0984 to 0.1298 with similar depleted mantle (DM; DePaolo, 1981) model ages from ~2.0 to 2.2 Ga. The Caracaraí and country rock gabbronorites have slightly higher $^{147}Sm/^{144}Nd$ ratios and DM model ages of 2.4 and 2.2 Ga, respectively. The concentrations of Sm and Nd vary respectively from 2.39 to 12.06 ppm in the anorthosite to 22.93 and 134.76 ppm in the biotite granite. The Caracaraí gabbronorite has very low concentrations at 0.49 ppm Sm and 1.66 ppm Nd, even lower than the country rock gabbronorite (3.65 and 14.51 ppm, respectively).

The calculated initial Nd isotope compositions of the four rock types of the Mucajaí-complex are slightly subchondritic. The anorthosite has namely the most radiogenic and the BG the least radiogenic value (initial ε_{Nd} values of −1.9 and −2.8 at 1525 Ma, respectively). The monzonite and biotite–hornblende granite have ε_{Nd} values of −2.0 and −2.3 at 1525 Ma, respectively. Given the external analytical uncertainty of ±0.4 ε_{Nd} units the initial Nd isotope compositions of the four rock-types overlap.

The crystallization age of the Caracaraí gabbronorite is not known but the initial ε_{Nd} value (+0.8) is nevertheless reported at the age of the

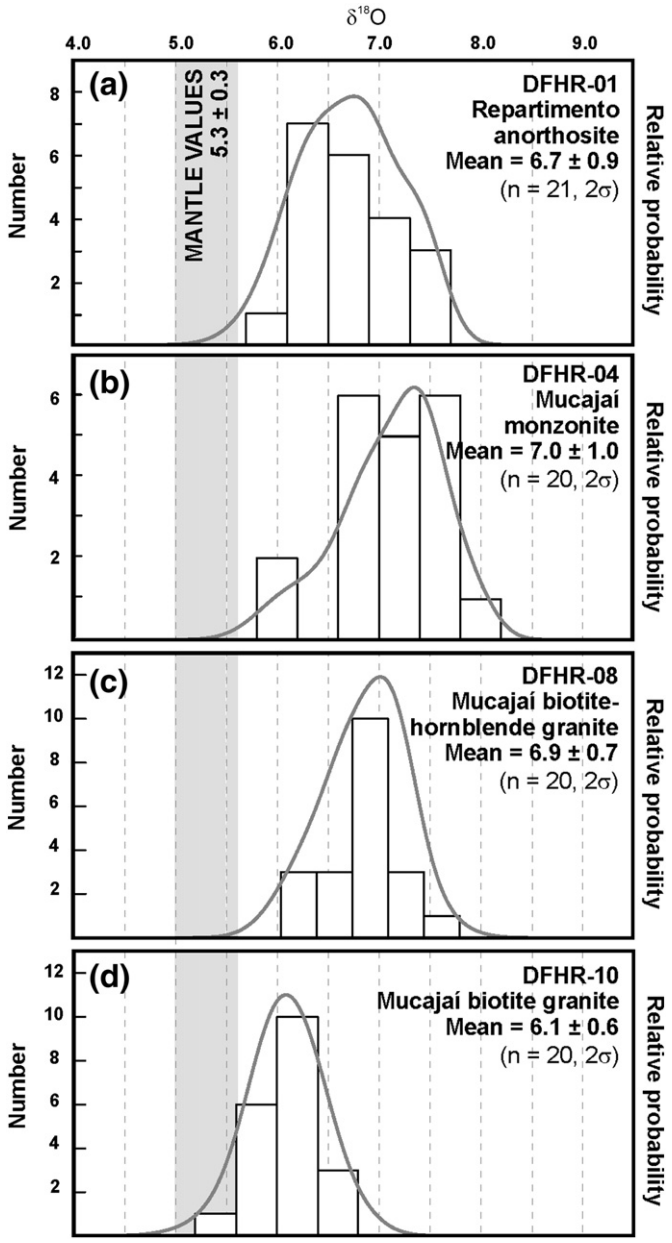

Fig. 7. Histograms and relative probability plots weighted with internal errors of the zircon oxygen isotope compositions of the samples of the Mucajaí complex relative to VSMOW (in ‰). Mean denotes the un-weighted average of *n* number of in situ analysis and is given with 2SD. Mantle values from Valley et al. (1998) are also shown.

Mucajaí complex for comparison (Table 4). Calculated at the age of the country rock gabbronorite ($\varepsilon_{Nd} = +2.0$ at 1.94 Ga), the Caracaraí has an initial ε_{Nd} value of +1.7. Extrapolated T_{DM}(Nd) ages for the Mucajaí rocks and the country rock gabbronorite are similar at ~1.97–2.16 Ga. The Caracaraí has a higher model age at ~2.43 Ga.

5.4. Zircon O isotopes

Oxygen isotope compositions of zircons from the four isotope samples are given in Table 5 and presented in Fig. 7. The zircons from the Repartimento anorthosite (DFHR-01) have an un-weighted mean $\delta^{18}O$ value of 6.7 ± 0.9‰ (2SD). The monzonite (DFHR-04) has a marginally higher un-weighted mean $\delta^{18}O$ value of 7.0 ± 1.0‰ (2SD). The zircons from the rapakivi granites of the Mucajaí complex have relatively low $\delta^{18}O$ values. The zircons from the Mucajaí biotite granite (DFHR-10) vary from 6.7‰ down to mantle values (5.4‰) with an un-weighted mean of 6.1 ± 0.6‰ (2SD) and the biotite–hornblende granite (DFHR-08) from 6.3 to 7.5 with an un-weighted mean $\delta^{18}O$ value of 6.9 ± 0.7‰ (2SD). Ranges in $\delta^{18}O$ values of the anorthosite and the monzonite are slightly higher than in the granites, but overlap between the rock-types is considerable (Fig. 7).

5.5. Zircon Lu–Hf isotopes

Hafnium isotope compositions of the studied zircons are given in Table 5 and illustrated in Figs. 8, 9, and 10. Where possible, the same portions of the zircon crystals were targeted as in the respective oxygen analysis.

$^{176}Lu/^{177}Hf$ ratios in the zircons from all the samples are typically low and range from ~0.0003 to ~0.002. $^{176}Yb/^{177}Hf$ ratios are generally low (~0.03) but elevated in some of the zircons (up to

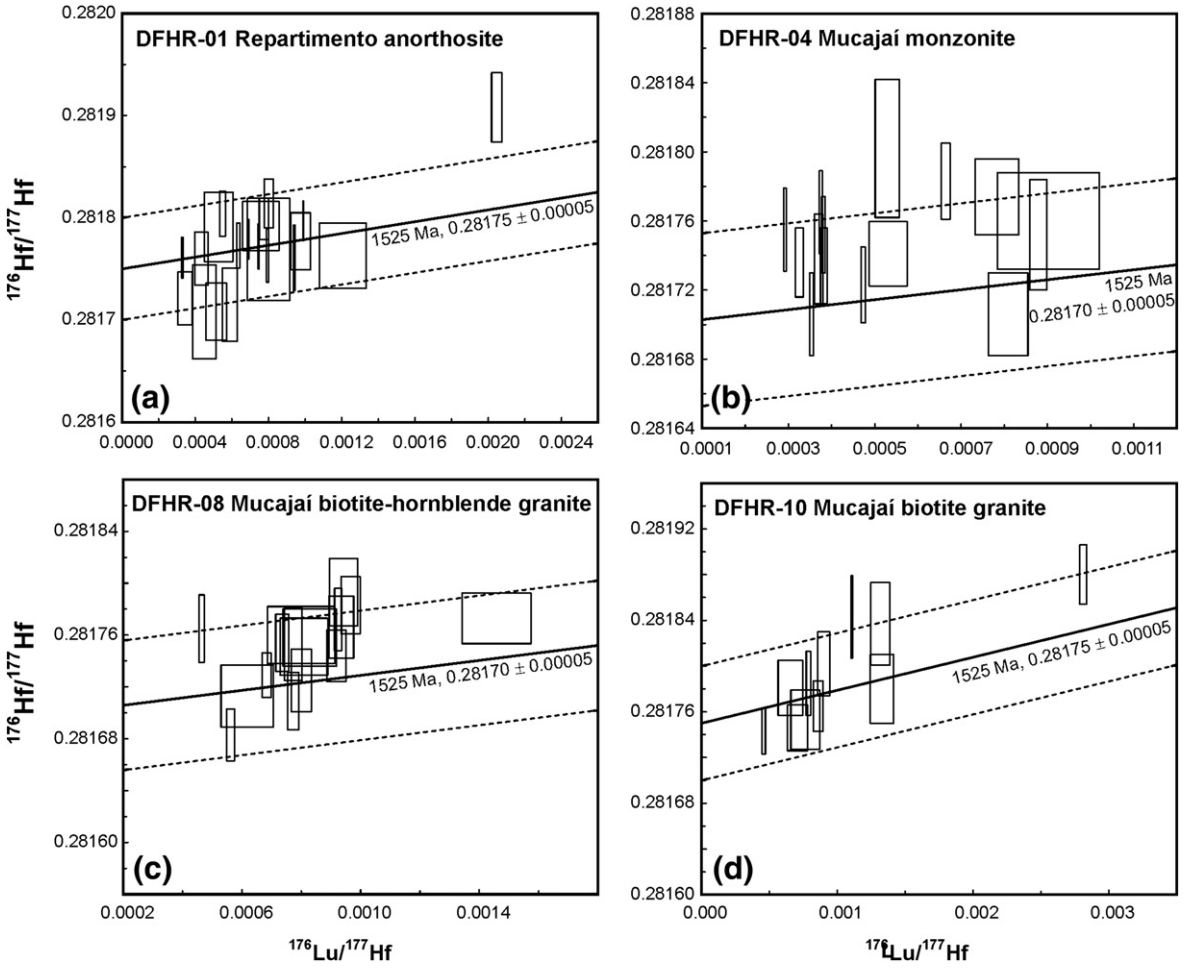

Fig. 8. Lu–Hf isochron diagrams of the samples from the Mucajaí complex. Calculated growth curves for best-fit initial $^{176}Hf/^{177}Hf$ ratios (±0.00005) at 1525 Ma show that the Hf isotope composition of all analyzed zircons can be explained by radiogenic growth or analytical uncertainties.

~0.1). Nevertheless, the values are well within the variation of the Temora-2 reference, which ranges up to $^{176}Yb/^{177}Hf$ of 0.12.

The initial Hf isotope compositions for the zircon analysis have been calculated at the crystallization ages indicated by the U–Pb ID–TIMS measurements for the corresponding rock types. Range in initial Hf isotope values is the largest in the zircons from the anorthosite (±2.6 ε_{Hf} at 2SD). The monzonite and the granites have lower 2SD ranges of ±2.0 (monzonite), ±1.8 (biotite–hornblende granite), and ±2.2 (biotite granite). All these variations fall roughly within the external ±2 ε unit range defined by the Temora-2 standard zircon and can, except for a single outlier (DFHR-01-16, Fig. 8a), be explained by in situ radiogenic growth with varying Lu/Hf ratios (Fig. 8). Un-weighted average initial ε_{Hf} values are all slightly negative and essentially indistinguishable within estimated uncertainty in all four samples (Fig. 9). The anorthosite (DFHR-01) has a negative average ε_{Hf} value of −2.2 (n = 21), whereas the biotite–hornblende granite (DFHR-08) has the lowest ε_{Hf} value at −3.1 (n = 17). The monzonite (DFHR-04) falls between of the previous ones with an average ε_{Hf} value of −2.9 (n = 16). The biotite granite (DFHR-10) has the least negative ε_{Hf} value of −2.0 (n = 11).

6. Discussion

6.1. The age of the Mucajaí complex

The crystallization ages of the Repartimento anorthosite (1526 ± 2 Ma) and the Mucajaí monzonite (1526 ± 2 Ma) and biotite–hornblende granite (1527 ± 2 Ma) are identical within error. The Mucajaí biotite granite is slightly younger at 1519 ± 2 Ma and is thus the latest magmatic phase of the complex.

Previous geochronological studies of the complex (Fraga et al., 2009a; Gaudette et al., 1996; Santos et al., 1999) provided a large array of Mesoproterozoic ages (from ca. 1585 to 1520 Ma). The SHRIMP age of 1527 ± 7 Ma reported by Santos et al. (1999) for the Repartimento anorthosite is indistinguishable from our determination but other previous studies reported older ages (Fraga et al., 2009a; Gaudette et al., 1996). The new data show that the magmatic activity in the Mucajaí complex was relatively short-lived and lasted at maximum 12 m.y. (1529 to 1517 Ma) within the younger end of the previously proposed range of ages. The majority of the rock types of the complex is coeval and the only resolvable age difference of 3 Ma is between the biotite granite and the remainder of the rock types of the complex.

The Mucajaí complex is coeval with the youngest group of rapakivi granites and associated rocks of the Fennoscandian shield (e.g., Rämö and Haapala, 2005). These include the 1.53–1.47 Ga Ragunda complex (Persson, 1999), some smaller granitic intrusions in Sweden (Mullnäset, 1526 ± 3 Ma; Mårdsjö, 1524 ± 3 Ma; and Nordsjö 1520 ± 3 Ma; Andersson et al., 2001), and the 1.52–1.50 Ga Mazury complex in northeastern Poland (Skridlaite et al., 2008; Wiszniewska et al., 2002).

6.2. Petrogenesis of the Mucajaí complex

The slightly subchondritic initial Nd (ε_{Nd} from −1.8 to −2.8; Fig. 6) and Hf (ε_{Hf} from ~0 to −5; Fig. 10) isotope compositions of the Mucajaí complex rocks support the previous conclusions of the involvement of a Paleoproterozoic crustal source component (Fraga et al., 2009a) in their

genesis either as the primary source or as a contaminant. The restricted range and relatively light oxygen isotope composition ($\delta^{18}O_{zir}$ ~5.5–8.0‰; Fig. 7) of the analyzed zircon suggests that this crustal component lacks major supracrustal input and is most likely dominantly plutonic in character. This fits well the observed field relations as the exposed country rocks of the complex are dominantly igneous granitic rocks and gneisses (Fraga et al., 2009a,b).

Typically the rapakivi granites of the Fennoscandian suite (Fig. 6a) and other similar associations (e.g., Nain Plutonic Suite; Emslie et al., 1994) exhibit slightly negative ε_{Nd} values that often overlap with the (overall, slightly more radiogenic) values of the associated basic rocks (Heinonen et al., 2010b; Rämö, 1991; Rämö et al., 1996). The initial Nd isotope pattern of Mucajaí is similar to that of the rapakivi granites and anorthositic rocks from the Fennoscandian association (Fig. 6a). However, in contrast to the relatively radiogenic source of the rocks of the Mucajaí complex (ε_{Nd} −2.8 to −1.9), the coeval (~1525 Ma) equivalent Fennoscandian rocks in Sweden have a pronounced Archean source component (ε_{Nd} from −8.9 to −4.8; Andersson et al., 2001; Fig. 6a).

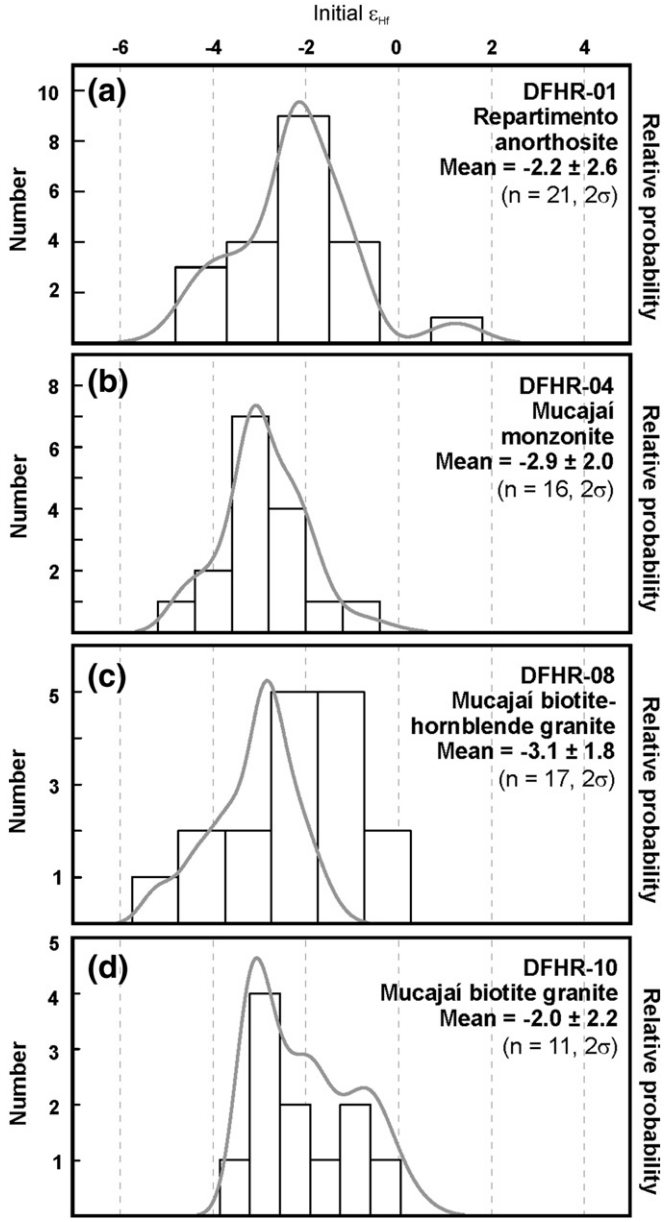

Fig. 9. Histograms and relative probability plots weighted with internal errors of the initial zircon Hf isotope compositions of the samples of the Mucajaí complex. Mean denotes the un-weighted average of *n* number of in situ analysis and is given with 2SD.

Monzodioritic and ferrodioritic rocks are a ubiquitous rock type associated with massif-type anorthositic complexes (e.g., Anderson et al., 2003; Frost et al., 2002; Heinonen et al., 2010b; Scoates and Chamberlain, 2003; Scoates et al., 1996). The discovery of monzodioritic rocks (samples DFHR-15 and DFHR-16) in Mucajaí further enhances comparison to other similar suites, for example the Ahvenisto complex in southeastern Finland (Alviola et al., 1999; Heinonen et al., 2010a,b) or the Laramie anorthosite complex in Wyoming (Anderson et al., 2003; Frost et al., 2002; Scoates and Chamberlain, 2003; Scoates et al., 1996).

Heinonen et al. (2010b) presented a tentative scenario for the petrogenesis of the ~1640 Ma Ahvenisto complex, modified from the models of Emslie et al. (1994), Mitchell et al. (1995), and Frost et al. (2002) based on similar plutonic suites in Laramie (Wyoming) and Nain (Labrador). The lack of intermediate rock compositions in Ahvenisto led Heinonen et al. (2010b) to propose separate magmatic sources for the silicic and basic rocks, and a common fractionation history for the olivine-bearing gabbroic rocks, anorthosites and monzodiorites of the complex. However, if this scenario is extended to the Mucajaí complex, the role of the monzonitic rocks becomes problematic as no equivalent compositions are known from Ahvenisto.

Scoates and Chamberlain (2003) presented a comprehensive model for the relationship between monzodioritic and monzonitic rocks of the Laramie anorthosite complex. According to Scoates and Chamberlain (2003), the Laramie monzonites represent fractionates of a monzodioritic (or ferrodioritic) precursor, which in itself is a residual liquid after anorthosite fractionation. The monzonites in Mucajaí fall on similar geochemical trends compared to the equivalent rocks in Laramie (Figs. 3 and 11; Scoates and Chamberlain, 2003) with one notable exception. The rocks of the ferrodioritic-monzonitic lineage of Laramie show effects of possible plagioclase accumulation only in the last phase of fractionation (accumulation trend C in Fig. 11a), whereas Mucajaí seems to have been affected earlier in the fractionation sequence (trend A in Fig. 11a). The monzodiorites discovered from Mucajaí would therefore not represent primary compositions of the monzodioritic fractionation but partial cumulates derived from the original fractionation lineage. Scoates et al. (1996), Frost et al. (2002), and Anderson et al. (2003) extended the lineage also to the coeval granitic rocks in Laramie, but Scoates and Chamberlain (2003) considered them to be of separate origin. Also the rapakivi granites of the Ahvenisto complex are more likely to be derived from a crustal source rather than by direct fractionation of mantle material (Heinonen et al., 2010a,b; Rämö, 1991).

The diverse range of petrogenetic processes suggested for the similar plutonic suites in these localities eventually boils down to tracing the influence of different sources (mantle and crust) on the generated rocks. The coupled zircon in situ O–Hf dataset obtained from the Mucajaí complex could ideally be utilized in resolving this source controversy at least in the northern Brazilian suite. Some magmatic processes (e.g., assimilation or mixing) that might be difficult to distinguish in bulk rock isotopic analysis can be traced by detailed isotopic analysis of zircon (e.g., Kemp et al., 2007). Local saturation of zircon at multiple stages during crystallization may generate isotopically heterogeneous mineral populations that are capable of recording compositional changes of a mantle-derived magma undergoing assimilation of an isotopically contrasting crustal contaminant.

This phenomenon is quite pronounced in the zircons from the anorthositic rocks of the 1540–1670 Ma Finnish rapakivi association (Heinonen et al., 2010a). The basic rocks clearly record a depleted mantle signature, which is manifested in the significantly broader variation (±>5 ε units) of initial zircon Hf isotope compositions compared to the coeval granitic rocks (±~2 ε units). Such variation is observed neither in the zircon hafnium nor zircon oxygen isotope composition of the Repartimento anorthosite (Figs. 7a and 9a). Though nominally higher than in the granites, the range in initial ε_{Hf} values of the anorthosite (±2.6) is not large enough to be generated

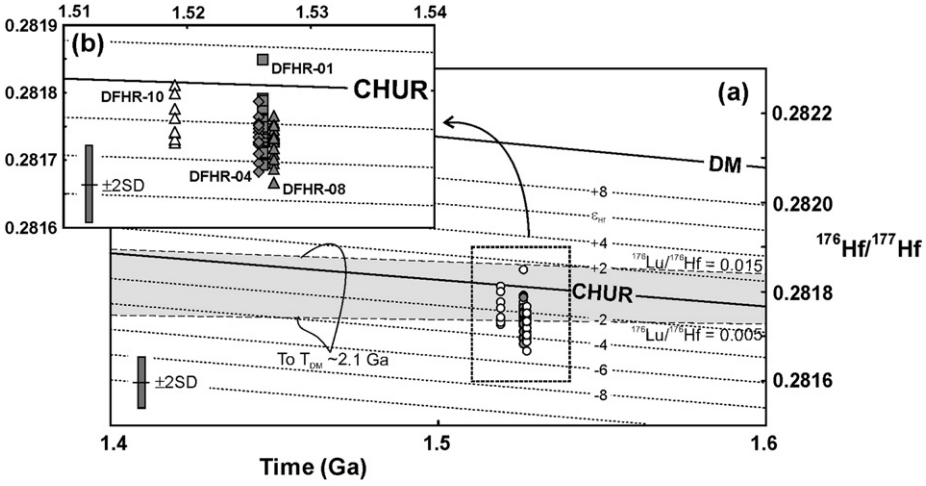

Fig. 10. Age vs. $^{176}Hf/^{177}Hf$ diagram of the Mucajaí samples with CHUR (Chondritic Uniform Reservoir; Bouvier et al., 2008) and DM (Depleted Mantle; Griffin et al., 2000) models shows the unradiogenic Hf isotope composition of the magmas at the time of crystallization. DFHR-01 and DFHR-04 with the same age (1526 Ma) have been slightly offset in (b) for the clarity of the plot. Back-calculated Hf isotope evolution of the enclosing country rocks is also depicted at average crustal $^{176}Lu/^{177}Hf$ ratios from 0.005 to 0.015 (Griffin et al., 2002) assuming T_{DM} of ~2.1 Ga (from Nd isotopes in Fraga et al., 2009a). See the text for further details.

by other than analytical causes (external 2SD error of ~±2 ε units). The zircon Hf isotope compositions in the Repartimento anorthosite do not thus imply the existence of a depleted mantle source to the same extent as the Finnish counterparts do (Heinonen et al., 2010a).

Even though the studied samples have Hf–O isotopic compositions that overlap within error, and evidence of contamination (crustal assimilation or mixing) of a mantle-derived magma cannot be seen, some variations observed in the data require more detailed explanations. Steeper REE pattern of the biotite granite (DFHR-10) suggests that it is more fractionated compared to the other granites of the complex (Fraga et al., 2009a; Fig. 4c), as would be expected for the most evolved rock type in the complex. However, the biotite granite has the lowest (most "mantle-like") $\delta^{18}O$ signature (6.1 ± 0.6‰; Figs. 7 and 12) and ranges to the highest initial ε_{Hf} values (up to ε_{Hf} ~ −0.2; Figs. 9, 10, and 12) among the studied samples. This observation is difficult to fit into the model of Fraga et al. (2009a), in which the granites are considered to represent fractionates of a common parental magma.

The lower $\delta^{18}O_{zir}$ values in the biotite granite are most likely not caused by mass fractionation effects during crystallization, as approximate calculated $\Delta^{18}O_{melt\text{-}zircon}$ values are higher for the biotite–hornblende granite than for the biotite granite regardless of the absolute crystallization temperature range (Fig. 13a). Approximate $\delta^{18}O_{melt}$ values calculated for the samples indicate that an implausible liquidus temperature difference of >200 °C would be needed to crystallize the observed ranges of $\delta^{18}O_{zir}$ from a granitic magma homogeneous in oxygen isotopes (Fig. 13b). This implies that the $\delta^{18}O$ range reflects actual magmatic variation and is not caused by changes in oxygen isotope fractionation during crystallization.

Four genetic factors may have contributed to the isotopic difference observed in the granites: (1) the crystallizing granitic magma chamber was intruded by a pulse of juvenile mantle-derived material (lower $\delta^{18}O$ and higher ε_{Hf}) after the biotite–hornblende granite crystallized and the biotite granite represents a later batch of granitic magma with isotope composition altered by this event. (2) The biotite–hornblende granite and the biotite granite were derived from similar, but isotopically slightly different crustal sources. (3) The biotite granite was more strongly contaminated by upper crustal material (with lower $\delta^{18}O$ and higher ε_{Hf}) than the biotite–hornblende granite. (4) The biotite granite has assimilated (cannibalized, e.g., Watts et al., 2010) hydrothermally altered (lowered $\delta^{18}O$) consanguineous granites. The first option is clearly precluded by major element geochemistry (Figs. 3 and 11) as none of the granitic rocks show significant deviation from the likely fractionation trends to lower SiO_2 values. The three other options can be considered as viable explanations.

The Hf or O isotope compositions of the country rocks of Mucajaí are not known; it is likely, however, that the crust is heterogeneous and thus has domains with varying isotope compositions. What would have been the Hf isotope composition of the enclosing ~1.94 Ga crustal rocks at the crystallization age of the Mucajaí complex (~1525 Ma) can be approximated by calculating evolution curves from their independently acquired average $T_{DM}(Nd)$ age of ~2.1 Ga (Fraga, 2002; Fraga et al., 2009a) and assumed Lu/Hf ratios (Fig. 10). The average crustal Lu/Hf ratio ($^{176}Lu/^{177}Hf = 0.015$; Griffin et al., 2002) gives clearly suprachondritic Hf isotope ratios at 1525 Ma (Fig. 10). To produce the initial isotope compositions observed in the Mucajaí complex, a more enriched crustal source with $^{176}Lu/^{177}Hf$ ratio of approximately 0.005 or alternatively a source with higher T_{DM} at average crustal Lu/Hf ratio (~0.015; Griffin et al., 2002) is needed. Either one of these options suggests that if the Paleoproterozoic lower crust is assumed as the primary source of the granitic rocks, it has a less radiogenic isotope composition from the rocks exposed on the surface.

The different Hf isotope compositions of the biotite–hornblende granite and the biotite granite could therefore be caused by derivation from different domains of the isotopically heterogeneous Paleoproterozoic crust (option 2, above). Differing $\delta^{18}O$ compositions with similar range as in the Mucajaí granites have also been reported from the granites of the Finnish rapakivi association ($\delta^{18}O_{zir}$ from ~6.0 to 8.5; Elliott et al., 2005). However, the values reported by Elliott et al. (2005) are from different intrusions and do not record possible internal variation within a magmatic system. The O isotope variation in the Finnish association is most likely geographical, so the results have been used to argue for differing crustal domains as the source of the granites. The results from Mucajaí show that comparable variation may be possible also within strictly consanguineous granites.

The modeled Hf isotope composition of the Mucajaí country rocks shows that the upper crust in the Mucajaí region may have a more juvenile Hf isotope signature than the lower crust, a feature required for the option number 3 above to be applicable. In option 3, lowered magmatic $\delta^{18}O$ values may be caused by interaction with hydrothermally altered crust as has been reported for example for some of the granites of the British Tertiary Igneous Province (Monani and Valley, 2003). Assuming a lower crustal source with a higher $\delta^{18}O$ and an upper crustal low $\delta^{18}O$ contaminant for the Mucajaí granites, it is

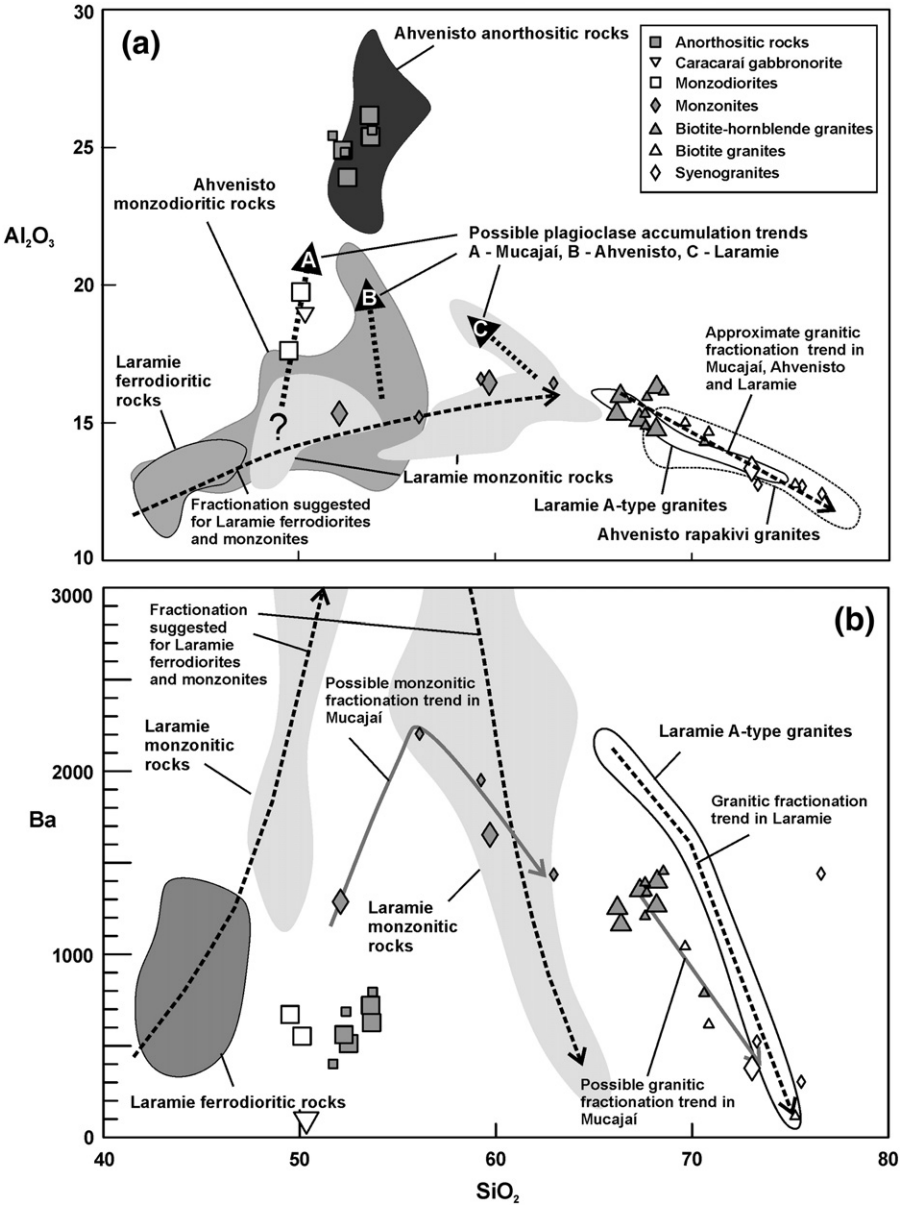

Fig. 11. Elemental geochemical constraints displayed on (a) SiO_2 (wt.%) vs. Al_2O_3 (wt.%) and (b) SiO_2 (wt.%) vs. Ba (ppm) diagrams for the petrogenesis of the Mucajaí complex, as well as due comparisons to the Ahvenisto (Heinonen et al., 2010b) and Laramie (Scoates and Chamberlain, 2003) complexes. Overall the rock types have similar geochemistry and the monzonites from the Mucajaí complex follow similar major element trends as in the Laramie complex (a). The monzodioritic rocks are elevated in Al_2O_3 relative to the equivalent Ahvenisto and Laramie rocks suggesting that they do not represent liquid compositions but include some cumulus plagioclase. Trace element trends show that the enrichment in the monzonitic rocks has most likely not reached similar levels as in Laramie and that the granitic differentiation has followed a somewhat differing trend (b).

possible that a longer upper crustal residence for the granitic magma could lead to the slightly lower $\delta^{18}O_{zir}$ values observed in the biotite granite, compared to the biotite–hornblende granite.

Also the Yellowstone caldera low $\delta^{18}O$ rhyolites (e.g., Watts et al., 2010 and references therein) that were formed late in the super eruption cycles could be considered as compositional equivalents to the late stage granites. In Yellowstone, so-called magmatic cannibalization is deemed as the most plausible reason of the late-magmatic shift in oxygen isotope composition (option 4, above). The low $\delta^{18}O$ signatures of the late-stage rhyolites are produced by remelting of earlier eruptive rocks of the same igneous system that have been altered by a high-temperature hydrothermal system.

The small but significant age difference between the biotite granite (~1520 Ma) and the rest of the Mucajaí complex (~1526 Ma) allows all three options considered above. However, cannibalization is evident only in O isotope compositions of rocks in subvolcanic environments, which cannot be confirmed in Mucajaí. Also the zircon Hf isotope signature that correlates with O isotopes suggests a truly open magmatic system. In addition, the whole-rock Nd isotope behavior seems to be decoupled from the O and Hf isotope systematics. On these grounds, option 4 is deemed unlikely as the cause of the observed isotope compositions. This leaves an isotopically heterogeneous source for the granites or a prolonged upper crustal residence time for the more evolved biotite granite as the most likely options.

The overlapping Nd, Hf and O isotope compositions of the rock types of the Mucajaí complex do not allow a definitive distinction between these models but clearly attest to the involvement of one or more crustal components in the petrogenesis of the Mucajaí complex. The new isotope data are therefore also compatible with the

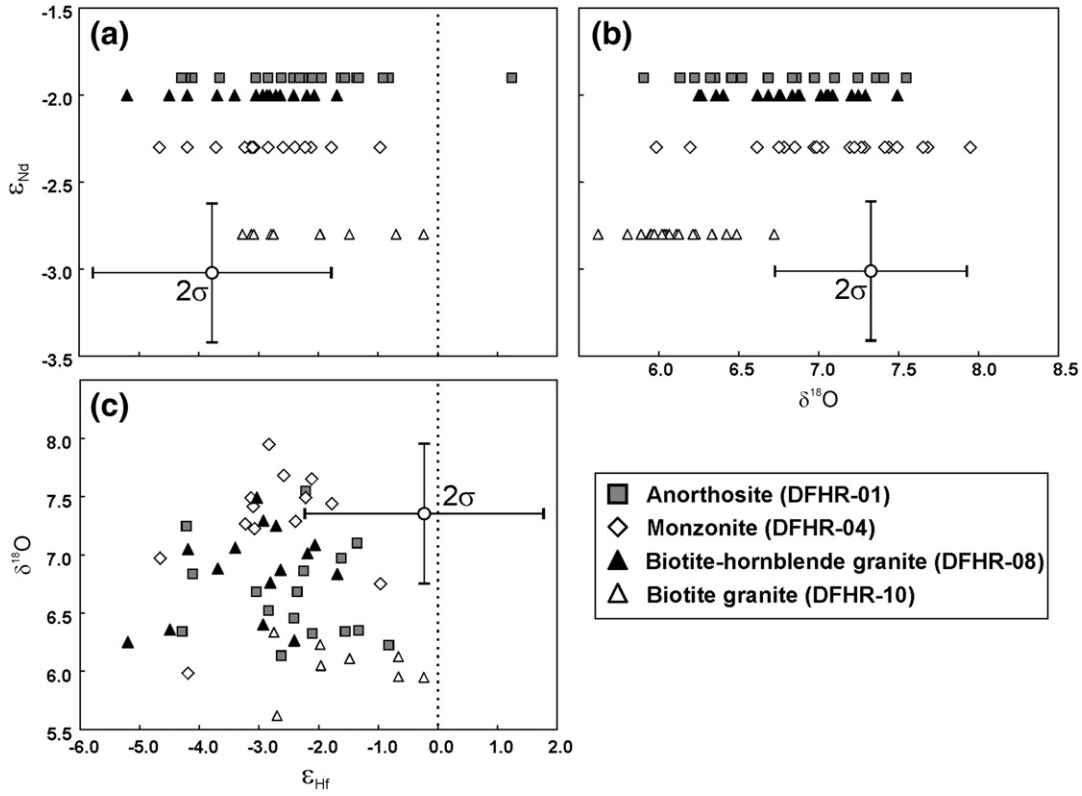

Fig. 12. Comparison of whole-rock Nd and zircon Hf–O isotope compositions of the Mucajaí rocks. The $\varepsilon_{Hf}(t)$ vs. $\varepsilon_{Nd}(t)$ (a), $\delta^{18}O$ vs. $\varepsilon_{Nd}(t)$ (b), and $\varepsilon_{Hf}(t)$ vs. $\delta^{18}O$ (c) diagrams show considerable overlap between the isotope compositions of the rock types. A weak signal of upper crustal contamination may be interpreted from the tentative correlation in hafnium and oxygen isotope compositions of zircon (c) in the biotite granite (DFHR-10). Maximum external 2σ error estimates for single analysis are plotted with each diagram.

prevailing two-source hypothesis (e.g., Emslie et al., 1994; mantle source for the anorthositic rocks and lower crustal source for the granitic rocks) postulated by Fraga et al. (2009a) for the Mucajaí complex. Based on the geochemical differences (Fig. 3; Fraga et al., 2009a) it is likely that the monzonitic rocks in Mucajaí are not related to the rapakivi granites by simple fractionation processes.

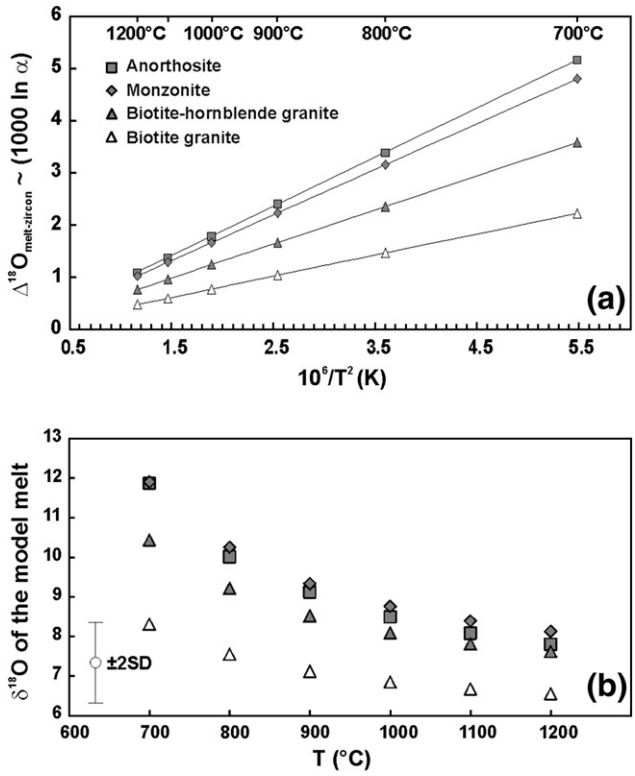

Fig. 13. Approximate $\Delta^{18}O_{melt\text{-}zircon}$ values calculated for normative whole-rock compositions (a) and inferred average $\delta^{18}O_{melt}$ compositions at different crystallization temperatures (b) for the Mucajaí complex. $A_{melt\text{-}zircon}$ (‰K^2) values were calculated after mineral values from Valley (2003).

The effect of possible mixing and mingling of mafic and felsic melts on the monzonitic trends (Figs. 3 and 11) remains an unexplored possibility. Almost all major-element trends could for example be explained by accumulation of alkali feldspar from a felsic source into mafic (possibly monzodioritic) fractionates (i.e., Scoates et al., 1996). However, no field evidence of these magmatic interactions is known and a more comprehensive major and trace element data set, especially of the monzodioritic rocks to constrain the mafic end-member, would be needed to test this hypothesis in the Mucajaí complex.

6.3. The Caracaraí gabbronorite

The whole-rock Nd isotope composition of the Caracaraí gabbronorite at 1525 Ma is clearly more juvenile than that of the Mucajaí complex (Fig. 6a) and at 1940 Ma it overlaps with the country rocks from Fraga et al. (2009a) and the country rock gabbronorite DFHR-14. Without a reliable magmatic age and confronted with clearly differing geochemistry (Figs. 3, 4, and 11), the affinity of the Caracaraí gabbronorite to the Mucajaí complex cannot be incontestably discounted, but seems unlikely.

7. Conclusions

Most of the rock types in the Mucajaí complex (anorthosite, monzonite, biotite–hornblende granite) are dated at 1524–1529 Ma. The biotite granite on the northeastern flank of the complex is somewhat younger at 1519 ± 2 Ma. This shows that the duration of AMG magmatism in Mucajaí region has been, at most, 12 m.y., possibly less.

The slightly subchondritic initial Nd and Hf isotope compositions of all the rock types of the Mucajaí complex imply a major crustal source component in their parental magmas. Judging from the modeled country rock Hf isotope evolution, this source component was most likely less radiogenic than the Paleoproterozoic rocks exposed on the present surface. The $\delta^{18}O_{zir}$ values of the studied rocks are relatively low ($\delta^{18}O_{zir}$ 5.5–8.0‰) and, thus, do not record significant supracrustal input to the magmas. Therefore, the crustal source components involved have most likely been predominantly plutonic in character. Some O–Hf isotope heterogeneity is however observed: the isotope signature with relatively lower $\delta^{18}O_{zir}$ and more radiogenic zircon ε_{Hf} values in the biotite granite compared to the biotite–hornblende granite implies a different level of contamination or alternatively two isotopically slightly contrasting sources for the parental magmas of the granites. In general, this observation shows that there exists a strong crustal control on the isotopic composition of some massif-type anorthosite–rapakivi granite complexes and that it can be active also during the very last stages of their magmatic evolution.

The geochemical similarities in the rock types between the Ahvenisto (Finland), Laramie (Wyoming), and Mucajaí (Brazil) imply similar petrogenetic processes (anorthositic to monzonitic fractionation and crustal contamination of a mantle derived primary magma) were active in all complexes, but that they are not all represented in the incomplete material available from the Mucajaí complex.

Acknowledgments

This study was funded by the Academy of Finland project SA1215351. The paper is a contribution to the Brazilian Institute of Amazonia Geosciences (INCT program–CNPq/FAPESPA — Proc. 573733/2008-2). This paper is NordSIM contribution number 294 and number 24 from the Department of Geosciences, University of Oslo, Isotope Geology Laboratory. We acknowledge the help of the fantastic CPRM field team and Nelson Reis in Repartimento and the aid received from Siri Lene Simonsen at UiO, Tuula Hokkanen and Arto Pulkkinen at GTK, and Martin Whitehouse, Kerstin Lindén, and Lev Ilyinsky at NRM, Stockholm. Special thanks for analytical help go to Helena Korkka and Matti Kurhila at the University of Helsinki. The editorial effort of C.D. Frost and the insightful reviews by C.M. Morriset and an anonymous reviewer considerably clarified the message of the manuscript.

Appendix A. Supplementary data

Supplementary data to this article can be found online at doi:10.1016/j.lithos.2011.07.016.

References

Alviola, R., Johanson, B.S., Rämö, O.T., Vaasjoki, M., 1999. The Proterozoic Ahvenisto rapakivi granite massif-type anorthosite complex, southeastern Finland; petrography and U–Pb geochronology. Precambrian Research 95, 89–107.
Anderson, I.A., Frost, C.D., Frost, B.R., 2003. Petrogenesis of the Red Mountain pluton, Laramie anorthosite complex, Wyoming: implications for the origin of A-type granites. Precambrian Research 124, 243–267.
Andersson, U.B., Neymark, L.A., Billström, K., 2001. Petrogenesis of Mesoproterozoic (Subjotnian) rapakivi complexes of central Sweden: implications from U–Pb zircon ages, Nd, Sr and Pb isotopes. Transactions of the Royal Society of Edinburgh: Earth Sciences 92, 201–228.
Ashwal, L.D., 1993. Anorthosites. Springer Verlag, Berlin, Germany.
Bonin, B., 2007. A-type granites and related rocks: evolution of a concept, problems and prospects. Lithos 97, 1–29.
Bouvier, A., Vervoort, J., Patchett, P.J., 2008. The Lu–Hf and Sm–Nd isotopic composition of CHUR: constraints from unequilibrated chondrites and implications for the bulk composition of terrestrial planets. Earth and Planetary Science Letters 273, 48–57.
Brandão, R.L., Freitas, A.F.F., 1994. Serra do Ajarani, Folha NA.20-X-C-VI: Relatório Final. Companhia de Pesquisa de Recursos Minerais, Manaus. 153 pages.
Cordani, U.G., Fraga, L.M., Reis, N., Tassinari, C.C.G., Brito-Neves, B.B., 2010. On the origin and tectonic significance of the intra-plate events of Grenvillian-type age in South America: a discussion. Journal of South American Earth Sciences 29, 143–159.
Dall'Agnol, R., Dreher, A.M., Araujo, J.F.V., Abreu, A.S., 1975. Granito Surucucu. Anais 10th Conf. Geol. Interguianas. Departamento Nacional da Produção Mineral, Belém, pp. 340–388.
Dall'Agnol, R., Costi, H.T., Leite, S.A.A., Magalhães, M.S., Teixeira, N.P., 1999. Rapakivi granites from Brazil and adjacent areas. Precambrian Research 95, 9–39.
DePaolo, D.J., 1981. Neodymium isotopes in the Colorado Front Range and crust–mantle evolution in the Proterozoic. Nature 291, 193–196.
DePaolo, D.J., Wasserburg, G.J., 1976. Nd isotope variations and petrogenetic models. Geophysical Research Letters 3, 249–252.
Duchesne, J.C., Liégeois, J.P., Vander Auwers, J., Longhi, J., 1999. The crustal tongue melting model and the origin of massive anorthosites. Terra Nova 11, 100–105.
Elliott, B.A., Peck, W.H., Rämö, O.T., Vaasjoki, M., Nironen, M., 2005. Magmatic zircon oxygen isotopes of 1.88–1.87 Ga orogenic and 1.65–1.54 Ga anorogenic magmatism in Finland. Mineralogy and Petrology 85, 223–241.
Emslie, R.F., Hamilton, M.A., Thériautl, R.J., 1994. Petrogenesis of a Mid-Proterozoic anorthosite–mangerite–charnockite–granite (AMCG) complex: isotope and chemical evidence from the Nain Plutonic suite. Journal of Geology 102, 539–558.
Fraga, L.M., 2002. A Associação Anortosito – Mangerito – Granito Rapakivi (AMG) do Cinturão Guiana Central e suas Encaixantes Paleoproterozóicas: Evolução Estrutural, Geocronologia e Petrologia. Doctoral thesis, Universidade Federal do Pará, Belém, Brazil.
Fraga, L.M.B., Dall'Agnol, R., Costa, J.B.S., Macambira, M.J.B., 2009a. The Mesoproterozoic Mucajaí anorthosite–mangerite–rapakivi granite complex, Amazonian craton, Brazil. The Canadian Mineralogist 47, 1469–1492.
Fraga, L.M., Macambira, M.J.B., Dall'Agnol, R., Costa, J.B.S., 2009b. 1.94–1.93 Ga charnockitic magmatism from the central part of the Guyana Shield, Roraima, Brazil: single-zircon evaporation data and tectonic implications. Journal of South American Earth Sciences 27, 247–257.
Frost, C.D., Frost, B.R., 1997. Reduced rapakivi-type granites: the tholeiite connection. Geology 25, 647–650.
Frost, C.D., Frost, B.R., 2011. On ferroan (A-type) granitoids: their compositional variability and modes of origin. Journal of Petrology 52, 39–53.
Frost, C.D., Frost, B.R., Bell, J.M., Chamberlain, K.R., 2002. The relationship between A-type granites and residual magmas from anorthosite: evidence from the northern Sherman batholith, Laramie Mountains, Wyoming, USA. Precambrian Research 119, 45–71.
Gaudette, H.E., Mendoza, V., Hurley, P.M., Fairbairn, H.W., 1978. Geology and age of the Parguaza rapakivi granite, Venezuela. Geological Society of America Bulletin 89, 1335–1340.
Gaudette, H.E., Olszewski, J.R., Santos, J.O.S., 1996. Geochronology of Precambrian rocks from the northern part of Guiana Shield, State of Roraima, Brazil. Journal of South American Earth Sciences 9, 183–195.
Gibbs, A.K., Barron, C.N., 1993. The Geology of the Guiana Shield. Oxford University Press, Claredon Press, New York. 245 pages.
Griffin, W.L., Pearson, N.J., Belousova, E., Jackson, S.E., van Achterbergh, E., O'Reilly, S.Y., Shee, S.R., 2000. The Hf isotope composition of cratonic mantle: LAM-MC-ICPMS

analysis of zircon megacrysts in kimberlites. Geochimica et Cosmochimica Acta 64, 133–147.
Griffin, W.L., Wang, X., Jackson, S.E., Pearson, N.J., O'Reilly, S., Xu, X., Zhou, X., 2002. Zircon chemistry and magma mixing, SE China: in-situ analysis of Hf isotopes, Tonglu and Pingtan igneous complexes. Lithos 61, 237–269.
Heinonen, A.P., Andersen, T., Rämö, O.T., 2010a. Re-evaluation of rapakivi petrogenesis: source constraints from the Hf isotope composition of zircon in the rapakivi granites and associated mafic rocks of Southern Finland. Journal of Petrology 51, 1687–1709.
Heinonen, A.P., Rämö, O.T., Mänttäri, I., Johanson, B., Alviola, R., 2010b. Formation and fractionation of high-Al tholeiitic magmas in the Ahvenisto rapakivi granite–massif-type anorthosite complex, Southeastern Finland. The Canadian Mineralogist 48, 969–990.
Kemp, A.I.S., Hawkesworth, C.J., Foster, G.L., Paterson, B.A., Woodhead, J.D., Hergt, J.M., Gray, C.M., Whitehouse, M.J., 2007. Magmatic and crustal differentiation history of granitic rocks from Hf–O isotopes in zircon. Science 315, 980–983.
Krogh, T.E., 1973. A low-contamination method for hydrothermal decomposition of zircon and extraction of U and Pb for isotopic age determinations. Geochimica et Cosmochimica Acta 37, 485–494.
Krogh, T.E., 1982. Improved accuracy of U–Pb zircon ages by creation of more concordant systems using an air-abrasion technique. Geochimica et Cosmochimica Acta 46, 637–649.
Longhi, J., 2005. A mantle or mafic crustal source for Proterozoic anorthosites? Lithos 83, 183–198.
Ludwig, K.R., 1991. PbDat 1.21 for MS-DOS: A Computer Program for IBM-PC Compatibles for Processing Raw Pb–U–Th Isotope Data.
Ludwig, K.R., 2003. Isoplot/EX 3. A Geochronological Toolkit for Microsoft Excel. Special Publication, 4. Berkeley Geochronological Center.
Mendoza, V.S., 1975. Estudios geoquímicos del no-tectonizado granito del Parguaza, Noroeste Guyana Venezuelana. 10th Conferência Geológica Interguianas, Belém, pp. 628–656.
Mitchell, J.N., Scoates, J.S., Frost, C.D., 1995. High-Al gabbros in the Laramie anorthosite complex, Wyoming: implications for the composition of melts parental to Proterozoic anorthosite. Contributions to Mineralogy and Petrology 119, 166–180.
Monani, S., Valley, J.W., 2003. Oxygen isotope ratios of zircon: magma genesis of low $\delta^{18}O$ granites from the British Tertiary Igneous Province, western Scotland. Earth and Planetary Science Letters 184, 377–392.
Montalvão, R.M.G. de, Muniz, M.C., Issler, R.S., Dall'Agnol, R., Lima, M.I.C., Fernandes, P.E.C.A., Silva, G.G., 1975. Geologia. Folha NB.20 — Boa Vista e parte das Folhas NA.21 — Tumucumaque, NB.20 — Roraima e NB.21. BRASIL. Departamento Nacional da Produção Mineral. Projeto RADAMBRASIL. DNPM, Rio de Janeiro.
Morse, S.A., 2006. Labrador massif anorthosites: chasing the liquids and their sources. Lithos 89, 202–221.
Neymark, L.A., Amelin, Yu.V., Larin, A.M., 1994. Pb–Nd–Sr isotope and geochemical constraints on the origin of the 1.54–1.56 Ga Salmi rapakivi granite–anorthosite batholith. Mineralogy and Petrology 50, 173–193.
Persson, A.I., 1999. Absolute (U–Pb) and relative age determinations of intrusive rocks in the Ragunda rapakivi complex, central Sweden. Precambrian Research 95, 109–127.
Pinheiro, S.S., Nunes, A.C.B., Camozzato, E., Andrade, F.B., Reis, N.J., Menezes, R.G., Carvalho, V.G.D., Wildner, W., 1981. Projeto Catrimani–Uraricoera. Relatório de progresso, vol. 1. CPRM, Manaus.
Rämö, O.T., 1991. Petrogenesis of Proterozoic rapakivi granites and related basic rocks of southeastern Fennoscandia: Nd and Pb isotopic and general geochemical constraints. Bulletin, 355. Geological Survey of Finland. 161 pages.
Rämö, O.T., Haapala, I., 2005. Rapakivi granites. In: Lehtinen, M., Nurmi, P.A., Rämö, O.T. (Eds.), Precambrian Geology of Finland — Key to the Evolution of the Fennoscandian Shield. Elsevier, Amsterdam, pp. 533–562.
Rämö, O.T., Huhma, H., Kirs, J., 1996. Radiogenic isotopes of the Estonian and Latvian rapakivi suites: new data from the concealed Precambrian of the East European Craton. Precambrian Research 79, 209–226.
Richard, P., Shimizu, N., Allégre, C.J., 1976. $^{143}Nd/^{146}Nd$, a natural tracer: an application to oceanic basalts. Earth and Planetary Science Letters 31, 269–278.
Santos, J.O.S., Reis, N.J., Hartmann, L.A., McNaughton, N.J., Fletcher, I.R., 1999. Associação Anortosito–Charnockito–Granito Rapakivi no Calimiano do Norte do Cráton Amazônico, Estado de Roraima: Evidências Obtidas por Geocronologia U–Pb (SHRIMP) em zircão e baddeleyíta. 6th Simpósio de Geologia de Amazônia, Manaus, pp. 503–506.
Santos, J.O.S., Hartmann, L.A., Gaudette, H.E., Groves, D.I., McNaughton, N.J., Fletcher, I.R., 2000. A new understanding of the Provinces of the Amazon Craton based on integration of field mapping and U–Pb and Sm–Nd geochronology. Gondwana Research 3, 453–488.
Santos, J.O., Potter, P.E., Reis, N.J., Hartmann, L.A., McNaughton, N.J., 2003. Age and regional stratigraphy of the Roraima Supergroup and Roraima Like outliers in Northern South America based on U–Pb geochronology. Bulletin of the Geological Society of America 115, 331–348.
Santos, J.O.S., Hartmann, L.A., Faria, M.S., Riker, S.R., Souza, M.M., Almeida, M.E., McNaughton, N.J., 2006. A compartimentação cráton Amazonas em províncias: avanços ocorridos no período 2000–2006. VI simpósio de Geologia de Amazônia, SBGEO-nucleo norte, cdrom.
Scherer, E., Münker, C., Mezger, K., 2001. Claibration of the lutetium–hafnium clock. Science 293, 683–687.
Scherer, E.E., Münker, C., Mezger, K., 2007. The Lu–Hf systematic of meteorites: consistent or not. Goldschmidt Conference Abstracts 2007: Geochimica et Cosmochimica Acta, 71, p. A888.
Scoates, J.S., Chamberlain, K.R., 2003. Geochronologic, geochemical and isotopic constraints on the origin of monzonitic and related rocks in the Laramie anorthosite complex, Wyoming, USA. Precambrian Research 124, 269–304.
Scoates, J.S., Frost, C.D., Mitchell, J.N., Lindsley, D.H., Frost, B.R., 1996. Residual-liquid origin for a monzonitic intrusion in a mid-Proterozoic anorthosite complex: the Sybille intrusion, Laramie anorthosite complex, Wyoming. GSA Bulletin 108, 1357–1371.
Skridlaite, G., Baginski, B., Whitehouse, M., 2008. Significance of 1.5 Ga zircon and monazite ages from charnockites in southern Lithuania and NE Poland. Gondwana Research 14, 663–674.
Söderlund, U., Patchett, P.J., Vervoort, J.D., Isachsen, C.E., 2004. The ^{176}Lu decay constant determined by Lu–Hf and U–Pb isotope systematics of Precambrian mafic intrusions. Earth and Planetary Science Letters 219, 311–324.
Stacey, J.S., Kramers, J.D., 1975. Approximation of terrestrial lead isotope evolution by a two stage model. Earth and Planetary Science Letters 78, 211–223.
Sun, S.S., McDonough, W.F., 1989. Chemical and isotopic systematics of oceanic basalts: implications for mantle composition and processes. In: Saunders, A.D., Norry, M.J. (Eds.), Magmatism in Ocean Basins: Geological Society of London Special Publication, 42, pp. 313–345.
Tassinari, C.C.G., Macambira, M.J.B., 2004. A evolução tectônica do cráton Amazônico. In: Mantesso-Neto, V., Bartoreli, A., Carneiro, C.D.R., Brito-Neves, B.B. de (Eds.), Geologia do Continente Sul-Americano — Evolução da Obra de Fernando Flávio Marques de Almeida, São Paulo, pp. 471–485.
Valley, J.V., 2003. Oxygen isotopes in zircon. Reviews in Mineralogy and Geochemistry 53, 343–385.
Valley, J.W., Kinny, P.D., Schulze, D.J., Spicuzza, M.J., 1998. Zircon megacrysts from kimberlite: oxygen isotope heterogeneity among mantle melts. Contributions to Mineralogy and Petrology 133, 1–11.
Watts, K.E., Leeman, W.P., Bindeman, I.N., Larson, P.B., 2010. Supereruptions of the Snake River Plain: two-stage derivation of low-$\delta^{18}O$ rhyolites from normal-$\delta^{18}O$ crust as constrained by Archean xenoliths. Geology 38, 503–506.
Whitehouse, M.J., Nemchin, A.A., 2009. High precision, high accuracy measurement of oxygen isotopes in a large lunar zircon by SIMS. Chemical Geology 261, 32–42.
Wiedenbeck, M., Hanchar, J., Peck, W.H., Sylvester, P., Valley, J., Whitehouse, M., Kronz, A., Morishita, Y., Nasdala, et al., 2004. Further characterization of the 91500 zircon crystal. Geostandards and Geoanalytical Research 28, 9–39.
Wiszniewska, J., Bagiński, B., Dörr, W., Walverde-Vaquero, P., Marhaine, D., 2002. U–Pb and Ar–Ar geochronology from the AMCG rock formation in the Mazury complex. Mineralogical Society of Poland — Special Papers 20, 221–224.